Estimating fibres' material parameter distributions from limited data with the help of Bayesian inference

H. Rappel[a,b], L.A.A. Beex[a,*]

[a] *Institute of Computational Engineering, Faculty of Science, Technology and Communication, University of Luxembourg, Maison du Nombre, 6, Avenue de la Fonte, 4364, Esch-sur-Alzette, Luxembourg.*
[b] *Computational & Multiscale Mechanics of Materials (CM3), Department of Aerospace and Mechanical Engineering, University of Liège, Quartier Polytech 1, Allée de la Découverte 9, B-4000 Liège, Belgium.*

Abstract

Numerous materials are essentially structures of discrete fibres, yarns or struts. Considering these materials at their discrete scale, one may distinguish two types of intrinsic randomness that affect the structural behaviours of these discrete structures: geometrical randomness and material randomness. Identifying the material randomness is an experimentally demanding task, because many small fibres, yarns or struts need to be tested, which are not easy to handle. To avoid the testing of hundreds of constituents, this contribution proposes an identification approach that only requires a few dozen of constituents to be tested (we use twenty to be exact). The identification approach is applied to artificially generated measurements, so that the identified values can be compared to the true values. Another question this contribution aims to answer is how precise the material randomness needs to be identified, if the geometrical randomness will also influence the macroscale behaviour of these discrete networks. We therefore also study the effect of the identified material randomness to that of the actual material randomness for three types of structures; each with an increasing level of geometrical randomness.

Keywords: stochastic parameter identification, fibrous materials, fabrics, foams, Bayesian inference, Bayes' theorem, copula, Gaussian copula, random networks

1. Introduction

Of all materials important for industry and society, some important ones are essentially discrete mesostructures and microstructures. Some examples are paper materials, open-cell metal foams, dry-woven fabrics and electrospun scaffolds. The mechanical behaviours of such materials are often described using computational models in which each fibre, yarn or strut is represented by a series of springs or beams. Examples are the work of Arnoux et al. [1] for bones and ligaments, the work of Ridruejo et al. [2] for glass fibre structures, the work of Kulachenko and Uesaka [3], Persson and Isaksson [4], Wilbrink et al. [5], Beex et al. [6], and Bosco et al. [7] for paper materials, the works of Delincé and Delannay [8], Badiche et al. [9] and Jung et al. [10] for open-cell metal foams, the works of Gao et al. [11], Boubaker et al. [12] and Beex et al. [13] for dry-woven fabrics and the work of Argento et al. [14] for elecrospun scaffolds.

A substantial amount of these discrete structures are intrinsically stochastic, which may be important to incorporate in their associated discrete models (see e.g. Sastry et al. [15], Wang et al. [16], Bronkhorst [17], Hatami-Marbini and Picu [18], Picu [19], Shahsavari and Picu [20] and Ban et al. [21]). Two types of stochastic aspects may be distinguished: stochastic geometries and stochastic mechanical behaviours of the base materials. Identifying both types of randomness is experimentally demanding because the structures and constituents are small.

*Corresponding author
Email address: lars.beex@uni.lu, l.a.a.beex@gmail.com (L.A.A. Beex)

Identifying stochastical geometries often involves the scanning of the structures with micro-CT scanners. An image analysis algorithm is then commonly applied, aiming to distinguish the individual fibres, yarns or struts in order to provide geometrical information such as their lengths, cross-sectional areas and orientations (e.g. Le et al. [22], Latil et al. [23], Sencu et al. [24]). Especially in order to distinguish the constituents in densely packed, small-scale structures, these algorithms need to be rather complex.

Some works that experimentally show and discuss stochastic aspects of the base materials of the discrete constituents are the work of Seth and Page [25] for paper materials and the work of Jung et al. [26] for open-cell metal foams. These studies show that a substantial difference in the mechanical behaviour can be observed between one constituent and another, but they do not present the actual distributions from which these behaviours are realisations. A possible reason for the fact that material parameter distributions are commonly not presented is that it requires the testing of a substantial number of fibres, yarns or struts, which are not easy to handle due to their small size.

The first aim of this contribution is therefore to propose a scheme that enables one to identify material parameter distributions using only a limited number of fibres, yarns or struts. We demonstrate the scheme for 20 constituents to be precise. The scheme assumes that all constituents can be described by the same material model and that the set of material parameters of each constituent is a realisation from some probability density function (PDF). For now, the scheme thus assumes that the material parameters are constant inside each constituent and the aim is to identify the parameters of the material parameter PDF. We apply the scheme to synthetically created measurements so that we can compare the identified values with the true ones.

The identification scheme requires four steps to be performed. First, fibres, yarns of struts need to be harvested and experimentally tested.

Second, the material parameters need to be identified separately for each constituent. We assume that the experimental tests are conducted in a well-controlled environment and hence, plenty of measurements are available for each tested constituent. Thanks to the abundance of available stress-strain data, the identification of the material parameters of each constituent is performed using the least squares method (LSM), in which an objective function in terms of the material parameters is minimised in order to determine their most appropriate values.

Third, univariate PDFs (i.e. single variable PDFs) are selected for each type of material parameter. The parameters of each univariate PDF are then identified based on the material parameter values identified in the previous step. The parameters of each univariate PDF are identified using Bayesian inference (BI), because not enough observations are available to allow a deterministic identification approach (we only have 20 observations). BI includes a regularisation that makes this separate identification problem well-posed.

Fourthly, the univariate PDFs together with their identified parameters are collected in one joint PDF, in which possible correlations between the univariate PDFs are incorporated. Mathematically combining the univariate PDFs is based on copulas, which come with their own parameter(s). Since again only 20 observations are available, the use of a deterministic approach for the identification of the copula parameters can be challenging and hence, we resort again to BI.

Bayesian frameworks treat observations as realisations from a probability model and their output are probability distributions in terms of the model parameters. Initially assumed parameter distributions need to be specified, which are then updated by inferring the observations. The result of this is again a probability distribution, which represents the user's uncertainty about the model parameters. This final PDF is called the posterior (distribution), whereas the initially assumed PDF is called the prior (distribution). In order to obtain statistical summaries of the posterior (e.g. at which parameter values the PDF is maximum), numerical frameworks are commonly employed.

Various studies can be found in which BI is used to identify material parameters. Examples that have focused on the identification of elastic material parameters are the works of Isenberg [27], Alvin [28], Beck and Katafygiotis [29], Marwala and Sibusiso [30], Gogu et al. [31], Koutsourelakis [32], Lai and Ip [33], Daghia et al. [34], Nichols et al. [35] and Gogu et al. [36]. Studies that have focused on the identification of elastoplastic parameters include the works of Most [37] and Rappel et al. [38, 39]. BI is also used to identify material parameters of hysteretic models [40, 41] and other nonlinear material models such as viscoelasticity

and creep [42–44].

As mentioned before, the univariate PDFs of each material parameter are coupled in one joint PDF by the use of copulas in this contribution. Copulas are defined as functions that link the joint cumulative distribution function (CDF) and the univariate CDFs. They allow to include the dependencies of several random variables on each other, resulting in a single multivariate distribution for all the material parameters.

Most often the parameters of the joint distribution (i.e. the parameters of univariate PDFs, as well as those of the copula) are identified by a two step identification scheme. Genest et al. [45] approximated the parameters of univariate distributions by empirical distribution (i.e. a nonparametric estimator of the CDF for a random variable) and used a maximum likelihood approach [46] to identify the parameters of the copula. Hürlimann [47] and Roch and Alegre [48] also employed a two step scheme, but with a maximum likelihood approach in both steps. Silva and Lopes [49] employed a full Bayesian approach for the identification of all unknown parameters in one step. However, the number of observations in their work is large compared to that in this contribution. Silva and Lopes also presented a comparison between one and two step methods, which showed a negligible difference between the point estimators of the one step scheme and the two step scheme.

Besides proposing the aforementioned identification scheme, this contribution also aims to answer the question of how accurate the material parameter PDF needs to be identified, if some level of geometrical randomness is present. To this purpose, we consider three types of virtual structures, each with an increasing level of geometrical randomness, and assess their macroscopic behaviour if the actual PDF is used and if the identified PDF is used. We investigate this for two responses of the base material: a damage model and an elastoplastic model. Geometrically linear Euler-Bernoulli beams are used to discretise the constituents in the virtual structures in a 2D setting.

The outline of this paper is as follows. Section 2 briefly discusses the material models. In Section 3, we discuss the identification scheme. In Section 4 we detail the generation and treatment of the virtual structures. In Section 5 we present some results, which are subdivided in those of the identification scheme itself and in how the distributions influence the macroscale behaviour of random network models. Finally, we present our conclusions (Section 6).

2. Material models

In this section, we briefly introduce the two material models that are used throughout this contribution. It is sufficient to express them in one dimension and without the use of the Poisson's ratio, because the identification scheme is applied to uniaxial (monotonically increasing) tensile tests and the virtual experiments use two-dimensional beam descriptions without shear deformation.

2.1. Damage

The first material model describes a linear elastic response until a failure strain is reached. When this failure strain is reached anywhere in the constituent (in the tensile tests considered in the identification scheme) or in a beam that represents a part of the constituent (in the virtual experiments), it fails entirely. No load will thus be transferred from that point onwards.

The Cauchy stress, σ, is expressed as follows in this material model:

$$\sigma = \big(1 - D(\kappa)\big) E \epsilon, \tag{1}$$

where D denotes the damage variable, which is a function of history variable κ. E denotes the Young's modulus and ϵ the linear strain.

We express the damage variable in terms of history variable κ as follows:

$$D(\kappa) = \begin{cases} 0 & \text{if } \kappa < \epsilon_f \\ 1 & \text{if } \kappa \geq \epsilon_f \end{cases}, \tag{2}$$

where ϵ_f denotes the failure strain. The following loading function and the Karush-Kuhn-Tucker (KKT) conditions [50] ensure that κ takes the largest strain value in a constituent or beam and that damage is irreversible:

$$g = \tilde{\epsilon} - \kappa, \tag{3}$$

with

$$\tilde{\epsilon} = \max_{\vec{x}} \left|\epsilon(\vec{x})\right|, \tag{4}$$

where $\vec{x}$ denotes the location vector to any material point in a constituent or beam. The KKT conditions read:

$$\dot{\kappa} \geq 0, \quad g \leq 0, \quad \dot{\kappa} g = 0. \tag{5}$$

It may be clear that in a monotonically increasing, uniaxial tensile test performed on a constituent, the strain is constant. Consequently, Eq. (4) can be simplified to:

$$\tilde{\epsilon} = \epsilon. \tag{6}$$

The stress-strain response during a monotonically increasing, uniaxial tensile test can then be written as:

$$\sigma = \begin{cases} E\epsilon & \text{if } \epsilon < \epsilon_f \\ 0 & \text{if } \epsilon \geq \epsilon_f \end{cases}. \tag{7}$$

2.2. Elastoplasticity

Second, we consider an elastoplastic material model with isotropic, linear hardening. In this material description, the linear strain, ϵ, is additively split in an elastic strain, ϵ_e, and a plastic strain, ϵ_p:

$$\epsilon = \epsilon_e + \epsilon_p. \tag{8}$$

The Cauchy stress, σ, is expressed as follows:

$$\sigma = E\epsilon_e. \tag{9}$$

The yield function reads:

$$f = \sqrt{\sigma^2} - \sigma_{y0} - H\tilde{\epsilon}_p, \tag{10}$$

where $\tilde{\epsilon}_p$ denotes the cumulative plastic strain, σ_{y0} the initial yield stress and H the plastic modulus. The relation between a change of the plastic strain and that of the cumulative plastic strain furthermore reads:

$$\dot{\epsilon}_p = \dot{\tilde{\epsilon}}_p \frac{\partial f}{\partial \sigma} = \dot{\tilde{\epsilon}}_p \, \mathrm{sgn}(\sigma), \tag{11}$$

where $\mathrm{sgn}(\cdot)$ denotes the sign function. The following KKT conditions finalise the material model:

$$\dot{\tilde{\epsilon}}_p \geq 0, \quad f \leq 0, \quad f\dot{\tilde{\epsilon}}_p = 0. \tag{12}$$

It may be clear that the stress-strain relation during monotonically increasing, uniaxial tension for this material model reads:

$$\sigma = \begin{cases} E\epsilon & \text{if } \epsilon < \frac{\sigma_{y0}}{E} \\ \sigma_{y0} + \frac{EH}{E+H}(\epsilon - \frac{\sigma_{y0}}{E}) & \text{if } \epsilon \geq \frac{\sigma_{y0}}{E} \end{cases}. \tag{13}$$

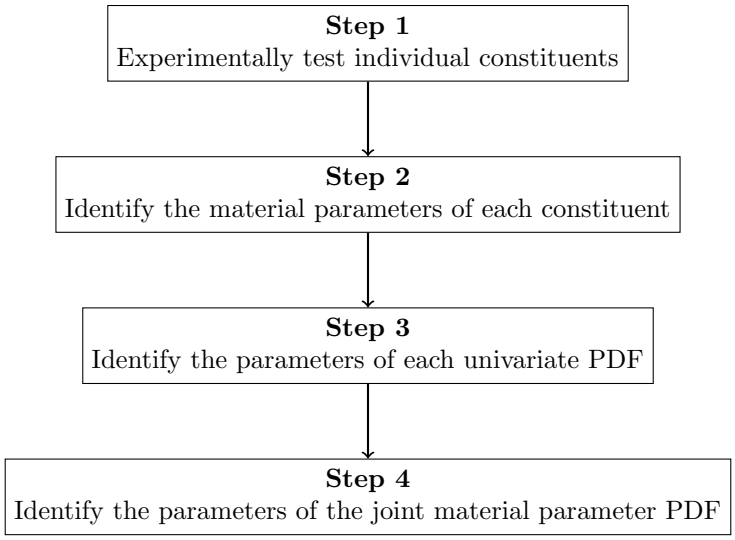

Figure 1: The steps of the identification scheme.

3. Identification scheme

In this section we detail the scheme to identify the parameters of the probability density function (PDF) from which it is assumed the material parameters of each specimen (i.e. tested constituent) are coming. First, the concept of the framework is discussed. Subsequently, the basics of Bayesian inference are discussed. Then, copulas are discussed as the mathematical tool to combine two or more univariate PDFs in one joint PDF. Finally, the two steps of the scheme in which BI and copulas are used are discussed in more detail.

3.1. Concept

The aim of the identification scheme is to experimentally test a relatively small number of fibres, yarns or struts and from those test results (i.e. stress-strain data), obtain the parameters of the material parameter PDF. We will achieve this by subdividing the identification problem in four steps, which are to be performed consecutively. These steps are discussed below and schematically illustrated in Fig. 1.

Step 1: Experimentally test individual constituents
First, some fibres, yarns or struts must be harvested and tested experimentally. We assume that 20 fibres are harvested and that these are separately tested in tension in a well-controlled environment. We thus obtain 20 stress-strain curves, which are necessary for the next step.

Step 2: Identify the material parameters of each constituent
Based on the stress-strain data obtained in the previous step, a material model must be selected in the current step and its parameters are separately identified for each constituent. We assume that a large number of stress-strain data is gathered during each test such that a deterministic identification approach based on the minimisation of an objective function is possible, i.e. the least squares method (LSM). The final result of the current step is thus a set of material parameters for each constituent. If we for instance assume the damage model of the previous section, we obtain 20 Young's moduli and 20 failure strains: two material parameters for each constituent. The material parameters of each constituent are necessary for the next step.

Step 3: Identify the parameters of each univariate PDF
In the third step, we select a univariate PDF for each type of material parameter (e.g. normal or beta distributions [46]) and identify the parameters of each univariate PDF separately. If we again assume the damage model of the previous section, we thus obtain two univariate PDFs: one for the Young's modulus and one for

the failure strain. As 20 observations (e.g. 20 Young's moduli) are not sufficient to identify the parameters of a univariate distribution deterministically, we employ Bayes' theorem to enable the use of assumed knowledge, which regularises the identification problem of the current step. The use of Bayes' theorem effectively means that a distribution of the univariate PDF's parameters is assumed and this distribution is updated by inferring each observation. We thus start the identification problem of the current step with the assumption of a distribution of the PDFs' parameters and the final result of BI is also a distribution in terms of the PDF's parameters (albeit corrected for the observations). We then use a numerical framework (Markov chain Monte Carlo, MCMC techniques) to explore the distribution of the univariate PDF's parameters to find their point estimates [51] (e.g. the mean vectors or MAP vectors). These point estimates are then considered as the identified parameter set of each univariate PDF, which are necessary for the fourth step.

Step 4: Identify the parameters of the joint material parameter PDF

In the last step, we take the univariate PDFs (including their identified parameters) and couple them together to form a single, joint PDF. The coupling of the univariate PDFs allows the incorporation of correlations and is mathematically performed here using a so-called copula. Different copula formulations can be distinguished and hence, the user has to select one. Since each copula comes with its own parameters, the identification problem in this fourth step thus aims to identify the copula parameters. Important to realise is that we again do not have enough information to employ a deterministic identification approach to identify the copula's parameters. Once more, we employ Bayes' theorem, requiring us to define an assumed PDF in terms of the copula parameters and inferring this PDF with the 20 observations. The resulting posterior needs to be numerically explored in order to determine the point estimates that represent the identified copula parameters.

It is worth mentioning that in principle the entire identification procedure can be performed in a single identification framework that is entirely based on Bayes' theorem. As the number of observations is small however, the MCMC algorithm (to numerically explore the final PDF in order to determine the point estimates) will not converge. Since we choose to obtain a unique joint PDF, we subdivide the identification approach into several identification problems. It is furthermore not very useful to consider the identification problem of Step 2 in a stochastic manner, because if we assume that a large number of stress-strain data for each constituent is available and the number of constituents is small, the uncertainty stemming from Step 2 is substantially small compared to the uncertainty stemming from Steps 3 and 4.

It is also worth noting that some clear assumptions are made in Steps 3 and 4: (i) the type of univariate PDFs (Step 3), (ii) the initially assumed distributions of the parameters of the univariate PDFs (Step 3), (iii) the type of copula (Step 4) and (iv) the initially assumed PDFs of the copula parameters (Step 4). The error induced by these assumptions cannot be evaluated to the best of the authors' knowledge, because few observations are available. If the number of tested constituents tends to infinity however, the error in the identified parameter values approximates zero (if the same PDFs and copula is selected as used to generate the material parameters, which in reality cannot be known in advance).

3.2. Bayesian inference

Bayesian inference (BI) is an identification procedure in which one fits a probability model to a set of data. The result of BI is a PDF (the so-called posterior). Assuming that $\mathbf{z} = \begin{bmatrix} z_1 & \cdots & z_{n_o} \end{bmatrix}^T$ denotes a vector of n_o observations and $\mathbf{p}$ a vector of n_p parameters which are to be identified, Bayes' formula reads:

$$\pi(\mathbf{p}|\mathbf{z}) = \frac{\pi(\mathbf{p})\pi(\mathbf{z}|\mathbf{p})}{\pi(\mathbf{z})} = \frac{1}{k}\pi(\mathbf{p})\pi(\mathbf{z}|\mathbf{p}), \tag{14}$$

where $\pi(\mathbf{p})$ denotes the prior PDF (i.e. the PDF that represents one's assumed prior knowledge about the parameters, e.g. the fact that the Young's modulus cannot be smaller than zero), $\pi(\mathbf{z}|\mathbf{p})$ denotes the likelihood function (i.e. the PDF that measures the likelihood that measurements $\mathbf{z}$ are observed, for a given set of parameter values $\mathbf{p}$), $\pi(\mathbf{p}|\mathbf{z})$ denotes the posterior PDF (i.e. the PDF that describes the probability to obtain parameters $\mathbf{p}$, for the given set of observations $\mathbf{z}$) and $\pi(\mathbf{z})$ is called the evidence. Since $\mathbf{z}$ is known,

the evidence is a constant number ($\pi(\mathbf{z}) = k \in \mathbb{R}^+$), which is thus independent of the parameters (i.e. the variables of interest). Since $\pi(\mathbf{z}) = k$, it suffices to write Eq. (14) as follows:

$$\pi(\mathbf{p}|\mathbf{z}) \propto \pi(\mathbf{p})\pi(\mathbf{z}|\mathbf{p}), \tag{15}$$

because the statistical summaries of the posterior, such as the mean, the MAP (i.e. the 'maximum-a-posteriori-probability' or the parameter values at which the posterior is maximal) and the covariance matrix (i.e. the matrix that measures the correlation between the parameters), are independent of scaling factor $\frac{1}{k}$.

Once the posterior is established, the statistical summaries of the posterior need to be determined. With the exception of a few cases, numerical frameworks need to be employed for this. Markov chain Monte Carlo (MCMC) techniques [52] are frequently employed to draw samples from the posterior PDF. The drawn samples can be used to approximate statistical summaries and predict new observations. Readers are referred to [39, 53] for more details.

3.3. Copulas

Nelsen [54] defines copulas as functions that join one dimensional marginal distributions to their joint, multivariate distribution. These functions are tools to model the dependencies of several random variables. We will discuss them in some more detail in this subsection.

Let $\mathbf{P} = \begin{bmatrix} P_1 & \cdots & P_n \end{bmatrix}^T$ be a random vector with joint cumulative distribution function (CDF) Π, and Π_i the marginal univariate CDF of P_i. According to Sklar's theorem [55], an n-dimensional copula C exists such that:

$$\Pi(p_1, \cdots, p_n) = C(\Pi_1(p_1), \cdots, \Pi_n(p_n)). \tag{16}$$

The joint PDF can then be obtained by differentiating Eq. (16) with respect to the random variables as follows:

$$\pi(p_1, \cdots, p_n) = c(\Pi_1(p_1), \cdots, \Pi_n(p_n)) \prod_{i=1}^{n} \pi_i(p_i), \tag{17}$$

where $c(u_1, \cdots, u_n) = \frac{\partial C(u_1, \cdots, u_n)}{\partial u_1 \cdots \partial u_n}$ with $u_i = \Pi_i(p_i)$ and $\pi_i(p_i)$ denotes the i^{th} marginal PDF.

Various types of copulas can be used to describe the dependencies of random variables [49], but we restrict ourselves to the Gaussian one. This entails that we write:

$$C(\mathbf{u}|\mathbf{\Gamma}_C) = \Phi_n(\Phi^{-1}(u_1), \cdots, \Phi^{-1}(u_n)|\mathbf{\Gamma}_C), \tag{18}$$

where again $u_i = \Pi_i(p_i)$, and $\mathbf{\Gamma}_C \in [-1, 1]^{n \times n}$ denotes the covariance matrix containing correlation parameters. These correlation parameters are called Pearson's ρ and each one is a measure for the linear relationship between two random variables [56]. Furthermore, $\Phi(\tilde{p})$ denotes the standard Gaussian CDF (i.e. $\tilde{p} \sim N(0, 1) = \frac{1}{\sqrt{2\pi}} \exp(-\frac{\tilde{p}^2}{2})$) and $\Phi_n(\tilde{\mathbf{p}}|\mathbf{\Gamma}_C)$ denotes the joint CDF of a multivariate Gaussian distribution with a zero mean vector and covariance matrix $\mathbf{\Gamma}_C$ (i.e. $\tilde{\mathbf{p}} \sim N_n(0, \mathbf{\Gamma}_C)$ with $\tilde{\mathbf{p}} = \begin{bmatrix} \tilde{p_1} & \cdots & \tilde{p_n} \end{bmatrix}^T$). [57] writes the density of the Gaussian copula as follows:

$$c(\mathbf{u}|\mathbf{\Gamma}_C) = \frac{1}{\sqrt{|\mathbf{\Gamma}_C|}} \exp\Big(-\frac{1}{2} \begin{bmatrix} \Phi^{-1}(u_1) & \cdots & \Phi^{-1}(u_n) \end{bmatrix} \times (\mathbf{\Gamma}_C^{-1} - \mathbf{I}) \times \begin{bmatrix} \Phi^{-1}(u_1) & \cdots & \Phi^{-1}(u_n) \end{bmatrix}^T \Big), \tag{19}$$

where $|\cdot|$ denotes the determinant and $\mathbf{I}$ the $n \times n$ identity matrix.

3.4. Details of Step 3

In this subsection and the next, we return to Steps 3 and 4 of the identification scheme and present them in more detail in the light of the previous discussions on BI and the Gaussian copula. In the current subsection, we focus on Step 3, meaning that we focus on how we use BI to identify the parameters of a univariate PDF based on 20 observations.

Let us assume that we have tested 20 constituents and identified the n_p types of material parameters for each constituent. We store the identified values of the first type of material parameters in a vector of length 20, $\overline{\mathbf{p}}_1$, the identified values of the second type of material parameters in a vector of the same length, $\overline{\mathbf{p}}_2$, and repeat this until we obtain n_p vectors of length 20.

In the current step, we separately focus on each type of material parameter, assume that they are realisations from some univariate PDF and identify the parameters of that univariate PDF. This means that we can now express Bayes' theorem for the material parameter of type i as follows:

$$\pi_{\text{post}}(\mathbf{p}_{i\text{PDF}}|\overline{\mathbf{p}}_i) \propto \pi_{\text{prior}}(\mathbf{p}_{i\text{PDF}})\pi_{\text{like}}(\overline{\mathbf{p}}_i|\mathbf{p}_{i\text{PDF}}), \tag{20}$$

where $\mathbf{p}_{i\text{PDF}}$ denote the parameters of the univariate PDF associated with the i^{th} type of material parameter and $\overline{\mathbf{p}}_i$ denote the observations for the current identification problem (e.g. if the i^{th} type of material parameter is the Young's modulus, $\overline{\mathbf{p}}_i$ contains the 20 Young's moduli identified in Step 2). The prior PDF is thus denoted by $\pi_{\text{prior}}(\mathbf{p}_{i\text{PDF}})$ and must be defined by the user. The posterior is denoted by $\pi_{\text{post}}(\mathbf{p}_{i\text{PDF}}|\overline{\mathbf{p}}_i)$. Likelihood function $\pi_{\text{like}}(\overline{\mathbf{p}}_i|\mathbf{p}_{i\text{PDF}})$ can straightforwardly be formulated using the product of the univariate PDF that is selected by the user:

$$\pi_{\text{post}}(\mathbf{p}_{i\text{PDF}}|\overline{\mathbf{p}}_i) \propto \pi_{\text{prior}}(\mathbf{p}_{i\text{PDF}}) \prod_{j=1}^{20} \pi_{\text{uni}}\Big((\overline{\mathbf{p}}_i)_j|\mathbf{p}_{i\text{PDF}}\Big), \tag{21}$$

where $(\overline{\mathbf{p}}_i)_j$ denotes the j^{th} component of $\overline{\mathbf{p}}_i$ (e.g. the j^{th} Young's modulus) and π_{uni} denotes the univariate PDF that must be selected by the user. The point estimates of all n_p posteriors are numerically estimated using MCMC techniques and are stored in n_p vectors $\overline{\mathbf{p}}_{1\text{PDF}}, \cdots, \overline{\mathbf{p}}_{n_p\text{PDF}}$.

Note that in principle the lengths of different vectors $\overline{\mathbf{p}}_{i\text{PDF}}$ may vary, since a different univariate PDF can be selected for each type of material parameter and each univariate PDF can come with its own number of parameters.

3.5. Details of Step 4

In the fourth step of the identification scheme, we take all the material parameters identified in Step 2 (stored in vectors $\overline{\mathbf{p}}_1, \cdots, \overline{\mathbf{p}}_{n_p}$, and for the ease of notation collect them in $\overline{\mathbf{p}}$) and the univariate PDFs including their parameters identified in Step 3 (stored in vectors $\overline{\mathbf{p}}_{1\text{PDF}}, \cdots, \overline{\mathbf{p}}_{n_p\text{PDF}}$ and for the ease of the notation collect them in $\overline{\mathbf{p}}_{\text{PDF}}$) and couple them with an assumed copula C, which comes with copula parameters $\boldsymbol{\rho}$. Hence, the aim of the current step is to identify the parameters in $\boldsymbol{\rho}$, which is of length $\frac{n_p(n_p-1)}{2}$ because the covariance matrix in a Gaussian copula is written as:

$$\boldsymbol{\Gamma}_C = \begin{bmatrix} 1 & \rho_{12} & \cdots & \cdots & \rho_{1n_p} \\ & 1 & \cdots & \cdots & \rho_{2n_p} \\ & \text{sym} & \ddots & \ddots & \vdots \\ & & & 1 & \rho_{(n_p-1)n_p} \\ & & & & 1 \end{bmatrix}, \tag{22}$$

where all values ρ_{ij} are stored in $\boldsymbol{\rho}$.

We can now express Bayes' theorem for the identification problem of the current step as follows:

$$\pi_{\text{post}}(\boldsymbol{\rho}|\overline{\mathbf{p}}, \overline{\mathbf{p}}_{\text{PDF}}) \propto \pi_{\text{prior}}(\boldsymbol{\rho})\pi_{\text{like}}(\overline{\mathbf{p}}|\overline{\mathbf{p}}_{\text{PDF}}, \boldsymbol{\rho}), \tag{23}$$

where we can decompose the likelihood function multiplicatively in terms of the joint PDF as follows:

$$\pi_{\text{like}}(\overline{\mathbf{p}}|\overline{\mathbf{p}}_{\text{PDF}},\boldsymbol{\rho}) = \prod_{i=1}^{20} \pi_{\text{joint}}\Big((\overline{\mathbf{p}}_1)_i,\cdots,(\overline{\mathbf{p}}_{n_p})_i|\overline{\mathbf{p}}_{\text{PDF}},\boldsymbol{\rho}\Big), \tag{24}$$

where the material parameters of the i^{th} tested specimen are denoted by $(\overline{\mathbf{p}}_1)_i,\cdots,(\overline{\mathbf{p}}_{n_p})_i$ (e.g. the i^{th} Young's modulus and failure strain) and the joint PDF for this specimen can be expressed as follows:

$$\pi_{\text{joint}}\Big((\overline{\mathbf{p}}_1)_i,\cdots,(\overline{\mathbf{p}}_{n_p})_i|\overline{\mathbf{p}}_{\text{PDF}},\boldsymbol{\rho}\Big) = c\Big(\Pi_{\text{uni}1}\big((\overline{\mathbf{p}}_1)_i|\overline{\mathbf{p}}_{1\,\text{PDF}}\big),\cdots,\Pi_{\text{uni}n_p}\big((\overline{\mathbf{p}}_{n_p})_i|\overline{\mathbf{p}}_{n_p\,\text{PDF}}\big)|(\boldsymbol{\Gamma}_C|\boldsymbol{\rho})\Big)\prod_{j=1}^{n_p}\pi_{\text{uni}j}\big((\overline{\mathbf{p}}_j)_i|\overline{\mathbf{p}}_{j\,\text{PDF}}\big). \tag{25}$$

The only remaining issues are to select a prior and subsequently, to determine the point estimates of the posterior using an MCMC algorithm [52].

4. Structural network models

As mentioned before, the accuracy of the identification scheme may not have a substantial effect on macroscopic network responses, if some form of geometrical randomness is also of influence. To investigate this, we use three types of two-dimensional network models; each with an increasing level of geometrical randomness. In this section, we detail the geometrical generation of the structural models, their discretisations, and the solution schemes associated with the two employed material models.

4.1. Geometries

The numerical network experiments in the results section are all performed on specimens resembling a dog-bone (see Fig. 2). The only boundary conditions prescribed are he displacements in vertical direction on the top and bottom of the domain, except for the first node on the bottom-left corner for which the displacement in horizontal direction is restrained as well. The cross-sectional shape of all discrete constituents is square, with the orientation of one edge of the square in out-of-plane direction. The cross-sectional dimensions are 1×1 mm^2.

In the first type of geometry, the discrete constituents are infinitely long (whilst still respecting the dog-bone shape), they are equally spaced (by parameter h in horizontal direction, i.e. in x-direction in Fig. 2) and they are oriented with an angle of $\theta = 45^\circ$ or $\theta = 135^\circ$. A typical geometry is schematically presented in Fig. 3(a). We will refer to this type of network as type A.

The second type of geometry is the same as the first geometry type with three differences: (i) the constituents have a finite length, (ii) the orientation of the constituents varies, and (iii) the constituents' centres of gravity are not perfectly aligned. We start the generation of these network geometries by taking the first network geometries and cutting each infinitely long constituent in finite constituents by sampling lengths from a uniform distribution with bounds $l_{\min}$ and $l_{\max}$. Then we change the orientation of each (finite) constituent by randomly sampling the orientation from a uniform distribution with bounds $45^\circ - \frac{1}{2}w_\theta$ and $45^\circ + \frac{1}{2}w_\theta$ or $135^\circ - \frac{1}{2}w_\theta$ and $135^\circ + \frac{1}{2}w_\theta$. Then, we relocate each constituent's centre of gravity by sampling its location from a bivariate, uncorrelated uniform distribution with bounds $x_c - \frac{1}{2}h_c$, $x_c + \frac{1}{2}h_c$, $y_c - \frac{1}{2}h_c$ and $y_c + \frac{1}{2}h_c$, where x_c and y_c denote the horizontal and vertical locations of the original centre of gravity, respectively. Finally, we investigate which constituents cross the specimen's borders and cut them accordingly. A typical geometry resulting from this generation is presented in Fig. 3(b). We will refer to this type of network as type B.

In the third and last type of geometry (in Fig. 3(c)), the length of the discrete constituents is again sampled from a uniform distribution with bounds $l_{\min}$ and $l_{\max}$. Their centres of gravity are randomly located in a rectangle of $(3\text{ mm} + 2l_{\max}) \times (6\text{ mm} + 2l_{\max})$, with the specimen centred in it. Their orientation

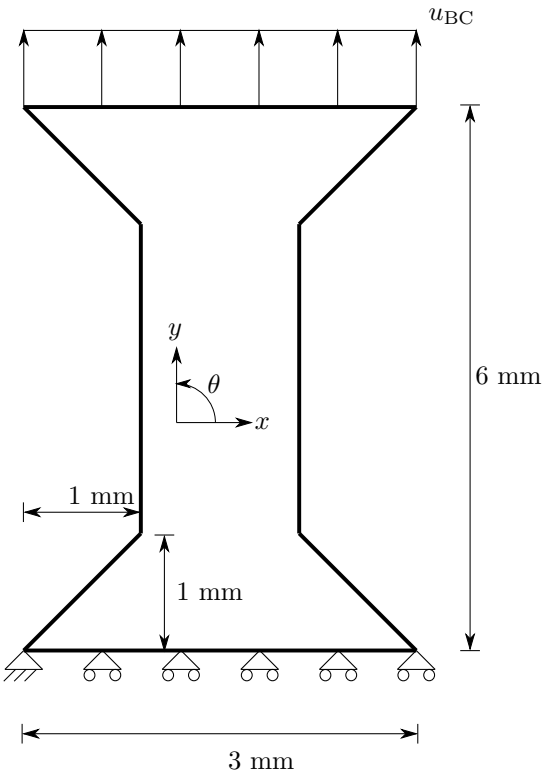

Figure 2: The shape, dimensions and boundary conditions of the specimens in the virtual experiments.

is completely random (i.e. their orientation is sampled from a uniform distribution with bounds 0° and 180°). If constituents cross the specimen's border, they are cut, and they are ignored if they are located entirely outside the specimen. We will refer to this type of network as type C.

4.2. Discretisations

After the geometries are created, each constituent is discretised by a string of two dimensional, geometrically linear, Euler-Bernoulli beams. If a constituent is not connected to any of the other constituents or if it is not connected to any of the specimen's edges to which boundary conditions are applied via other constituents, it is not discretised and hence, ignored. One beam is used for each constituent segment that is connected to two consecutive constituents. This means that if a constituent is connected to n other constituents, $n-1$ beams are used to discretise it and hence, n beam nodes are required. The beam nodes are placed at locations where the constituent crosses other constituents and hence, intersections between constituents are represented by a single beam node, entailing perfect connections between constituents (and thus between beams).

If the length of the smallest beam in the network is substantially small compared to the longest beam in the network, the stiffness matrix may become ill-posed. To avoid this problem, the length of the largest beam is measured and all beams that are smaller than 1% of the longest beam are removed and their nodes are unified. This process may involve the unification of more than two nodes. Finally, all beams that are only connected to one other beam are removed because they will not contribute to the structural response. A typical result of this discretisation strategy is shown in Fig. 4(b), together with the geometry in Fig. 4(a).

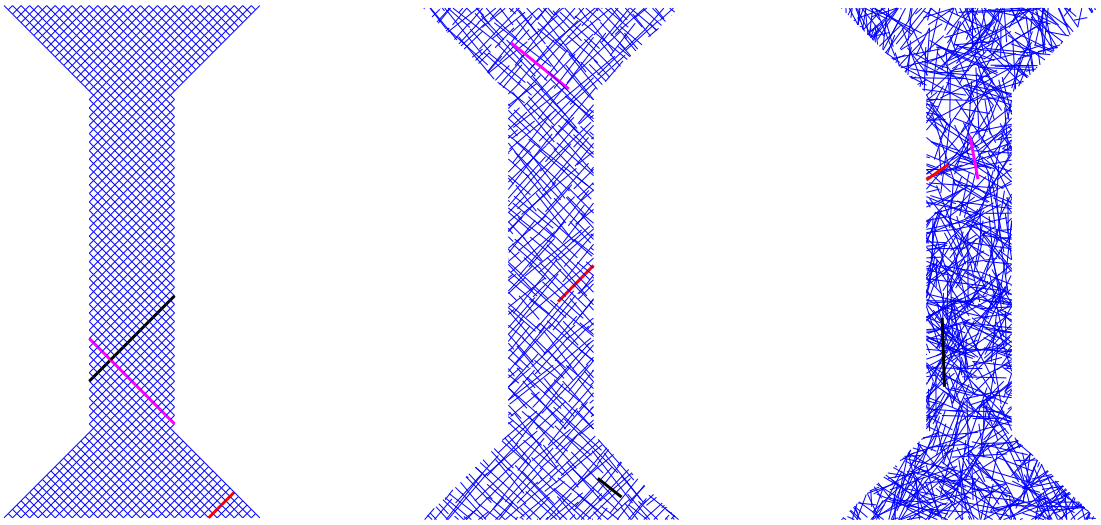

(a) (b) (c)

Figure 3: Schematic illustrations of the three types of networks. A few constituents are highlighted. The horizontal distance between the constituents in the type A and type B networks is $h = 0.1$ mm. The type B network is furthermore characterised by $l_{\min} = 0.3$ mm, $l_{\max} = 0.9$ mm, $w_\theta = 15°$ and $h_c = 0.04$ mm. The type C network geometry is characterised by $l_{\min} = 0.3$ mm, $l_{\max} = 0.9$ mm and by the fact that 2000 fibres are generated in domain $(3 \text{ mm} + 2l_{\max}) \times (6 \text{ mm} + 2l_{\max})$ with the specimen centred in it.

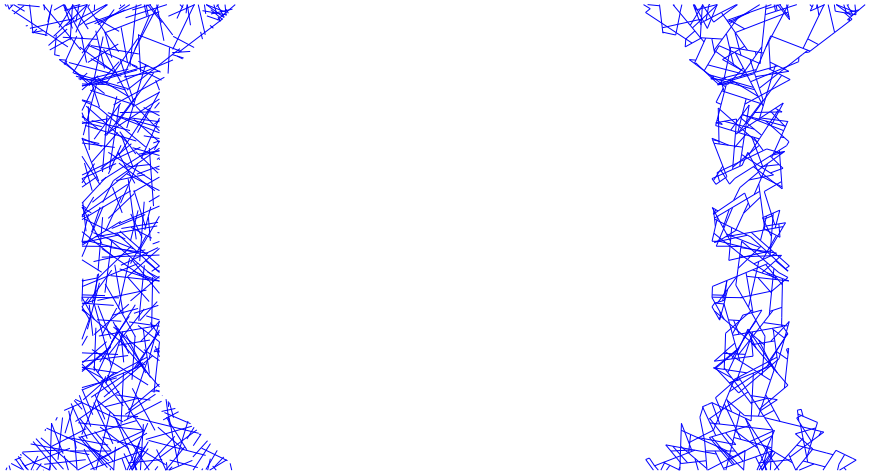

(a) (b)

Figure 4: A type C network geometry (a) and its beam discretisation (b). Note that we have used a significantly coarse network so that the effect of the discretisation can easily be observed.

4.3. Solution schemes

In this subsection, we briefly discuss the solution schemes for the EB beam network models associated with the two material models.

4.3.1. Damage

Solving the network model with the linear elastic-brittle fracture description starts with the application of an arbitrary value for u_{BC} in Fig. 2. After solving the linear system that results from this, we calculate in which of the beams the ratio between the occurring strain and the failure strain is the largest. This largest ratio will not equal one, but it should be at the moment that the beam fails. Since the material model is linear, we can scale this ratio directly to determine at which value of u_{BC} the beam fails. Similarly, we can also scale the reaction forces. After we have determined this, we remove the contributions of the failed beam to the stiffness matrix and again prescribe a value of u_{BC} and determine which of the beams is next to fail and at which value of u_{BC} and the reaction forces this would occur. We repeat this procedure until the sum of the reaction forces equals zero. This simple solution procedure is possible (instead of a true arc-length approach) due to the linearity of the model.

Eq. (4) states that the largest absolute strain occurring in a beam determines the value of κ and hence, the damage value for the entire beam. The maximisation problem of Eq. (4) is solved in a straightforward manner, because the largest absolute strain in a 2D EB beam occurs at the periphery of the beam, at its beginning or at its end end. Consequently, we only need to determine the strain at four locations per beam; two at the beginning and two at the end of each beam (left in Fig. 5).

4.3.2. Elastoplasticity

The network models using the elastoplastic material model are solved in a manner that is standard for elastoplasticity (e.g. using return mapping and the consistent tangent stiffness). We therefore do not detail them. The only issue worth mentioning is that we only use four integration points per beam in order to save computational efforts. These integration points are located at the centres of four equally sized, rectangular subdomains, as shown on the right in Fig. 5.

One may argue that these network models are far from perfect. We could for instance have used more integration points per beam for the elastoplastic material model. We also do not account for the fact that plasticity will lead to some form of localisation. We furthermore use cross-sectional dimensions that are too large to allow the use of geometrically linear EB beams. As the purpose of the virtual experiments in the next section is to compare the influence of the identified parameter distributions relative to the true parameter distributions if geometrical randomness is also present however, this comparison remains valid.

5. Results

This section presents the results for the identification scheme proposed in Section 3 as well as the results that show the effect of the different material parameter PDFs on the macroscale behaviour of the random network models. We start with the results of the parameter identification scheme.

5.1. Identification of the material parameter PDFs

In all results presented, we omit Steps 1 and 2 of the identification procedure and only consider Steps 3 and 4. This can be justified by assuming that an abundance of stress-strain measurements is obtained in Step 1, which makes the deterministic identification of the material parameters in Step 2 highly accurate.

We produce synthetic material parameters from two multivariate PDFs that are to be identified: one bivariate PDF for the damage model (in which Young's modulus E and failure strain ϵ_f are the material parameters) and a trivariate PDF for the elastoplastic model (in which Young's modulus E, initial yield stress σ_0 and hardening modulus H are the material parameters). We will refer to these PDFs as the 'true' PDFs. We draw 20 sets of material parameters from each true PDF. These sets of material parameters are considered to be the output of Step 2 and the observations in Step 3 (i.e. $\overline{\mathbf{p}}_i$).

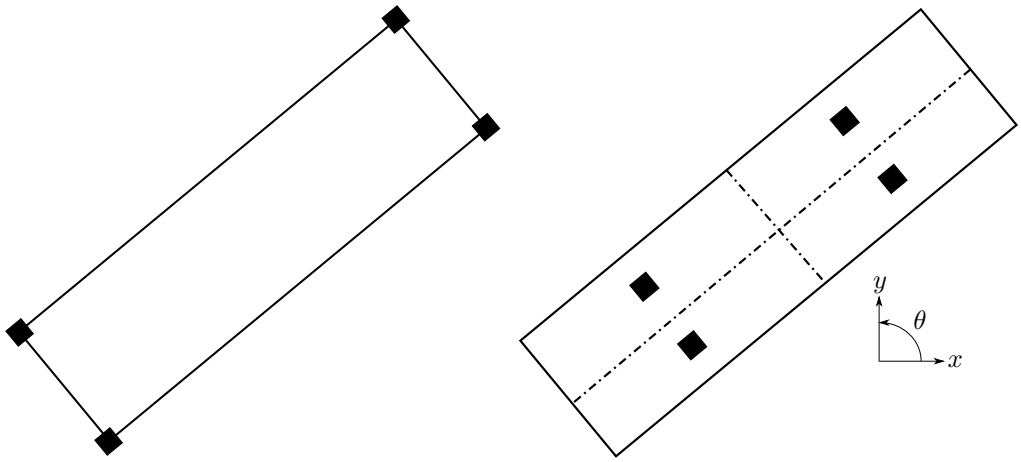

Figure 5: Left: the four locations at which the maximum strain in a $2D$ EB beam may occur (black squares). Right: the locations of the four integration points in a beam for the elastoplastic model (black squares).

Damage

In case of damage, we assume that the true bivariate PDF uses two univariate marginal PDFs which are four-parameter beta distributions of the following form:

$$\pi_{\mathrm{uni}\,i}(p_i|\mathbf{p}_{i\mathrm{PDF}}) = \frac{(p_i - a_{1i})^{\alpha_i - 1}(a_{2i} - p_i)^{\beta_i - 1}}{(a_{2i} - a_{1i})^{\alpha_i + \beta_i - 1} B(\alpha_i, \beta_i)},\ i = E \text{ and } \epsilon_f \tag{26}$$

where p_i denotes the material parameter (either E or ϵ_f), α_i and β_i denote the shape parameters of the univariate PDF and a_{1i} and a_{2i} the lower and upper bounds, respectively. Furthermore, $B(\cdot,\cdot)$ denotes the beta function. The two univariate PDFs are joined together with a Gaussian copula. The values that we have chosen for the true PDF are presented in Table 2, whilst the true PDF is graphically presented in Fig. 6(a).

Now we continue with the actual identification. We first need to assume the type of univariate marginal PDFs and copula. We choose to work with the same types as for the true PDF (i.e. both univariate marginal PDFs are four-parameter beta distributions and the copula is Gaussian), so that we can compare the identified values with true ones.

In addition to selecting the univariate PDFs and copula to be identified, we also need to select the priors for their parameters. It is important to realise that we only have a small number of observations (20), which easily makes the MCMC algorithm, used to explore the posterior PDF, fail to converge if non-informative priors are selected. We therefore need to select rather informative priors. This can easily be justified for the lower and upper bounds (a_1 and a_2) by the fact that one generally knows the type of base material. We have furthermore used the mean value and the standard deviation of the observations to construct the prior for the shape parameters (α and β). (Note that both the mean value and the standard deviation of the four-parameter beta distribution are functions of α, β, a_1 and a_2.)

The priors assigned to the parameters of the marginal univariate PDFs are in the following form:

$$\pi((\mathbf{p}_{i\mathrm{PDF}})_j) \propto \begin{cases} \exp\Big(- \frac{(p_{i\mathrm{PDF}})_j - \overline{(\mathbf{p}_{i\mathrm{PDF}})_j}^{\mathrm{prior}})^2}{2 s^2_{(\mathbf{p}_{i\mathrm{PDF}})_j}} \Big) & \text{if } (\mathbf{p}_{i\mathrm{PDF}})_j \geq 0 \\ 0 & \text{otherwise} \end{cases}, \tag{27}$$

where $(\mathbf{p}_{i\mathrm{PDF}})_j$ denotes the j^{th} parameter of the marginal univariate PDF for the i^{th} type of material parameter. In other words, j refers to α, β, a_1 or a_2 and i to E or ϵ_f. Furthermore, $\overline{(\mathbf{p}_{i\mathrm{PDF}})_j}^{\mathrm{prior}}$ and $s_{(\mathbf{p}_{i\mathrm{PDF}})_j}$ are the prior's mean value and standard deviation, respectively. We assume the prior for the

Table 1: Damage: the chosen values for the parameters that define the assigned priors.

$\overline{\alpha}_E^{\text{prior}}$	2	$\overline{\alpha}_{\epsilon_f}^{\text{prior}}$	3	$\overline{\rho}_{E\epsilon_f}^{\text{prior}}$	0.9
s_{α_E}	1	$s_{\alpha_{\epsilon_f}}$	1	$s_{\rho_{E\epsilon_f}}$	0.3
$\overline{\beta}_E^{\text{prior}}$	15	$\overline{\beta}_{\epsilon_f}^{\text{prior}}$	7		
s_{β_E}	5	$s_{\beta_{\epsilon_f}}$	2.3333		
$\overline{a}_{1E}^{\text{prior}}$ (GPa)	170	$\overline{a}_{1\epsilon_f}^{\text{prior}}$	0.0008		
$s_{a_{1E}}$ (GPa)	56.67	$s_{a_{1\epsilon_f}}$	2.6667×10^{-4}		
$\overline{a}_{2E}^{\text{prior}}$ (GPa)	270	$\overline{a}_{2\epsilon_f}^{\text{prior}}$	.0021		
$s_{a_{2E}}$ (GPa)	90	$s_{a_{2\epsilon_f}}$	7×10^{-4}		

Table 2: Damage: the true values and the identified MAP estimates.

α_E	β_E	a_{1E} (GPa)	a_{2E} (GPa)	α_{ϵ_f}	β_{ϵ_f}	$a_{1\epsilon_f}$	$a_{2\epsilon_f}$	$\rho_{E\epsilon_f}$
True values								
4	10	150	300	2	6	0.001	0.0019	0.7071
MAP estimates								
2.5786	8.3413	154.3811	365.6955	2.8056	7.3160	0.001	0.0021	0.6120

copula parameter (i.e. $\rho_{E\epsilon_f}$) to be in the same form:

$$\pi(\rho_{E\epsilon_f}) \propto \begin{cases} \exp\Big(-\frac{(\rho_{E\epsilon_f}-\overline{\rho}_{E\epsilon_f}^{\text{prior}})^2}{2s^2_{\rho_{E\epsilon_f}}}\Big) & \text{if } -1 < \rho_{E\epsilon_f} < 1 \\ 0 & \text{otherwise} \end{cases}. \tag{28}$$

The chosen values for the means and standard deviations are presented in Table 1.

By substituting the priors in Eqs. (21) and (23), the posterior is obtained. We use the adaptive Metropolis method [58] to draw samples from the posterior and hence, to obtain the statistical summaries such as the MAP. For each identification process 500×10^3 samples are drawn from the posterior whilst burning the first 30% of the samples. We have also imposed the constraint $a_1 < a_2$ in the sampling procedure. This entails that the samples that do not abide this constraint are rejected in the MCMC process.

The MAP estimates of the joint PDF are given in Table 2. Fig. 6 furthermore shows the true joint PDF and the identified joint PDF with and without correlation (i.e. with and without the copula) that correspond with these MAP estimates. One can observe that the identified joint PDF is somewhat wider than the true PDF, but substantially more accurate and less wide than the identified joint PDF without correlation.

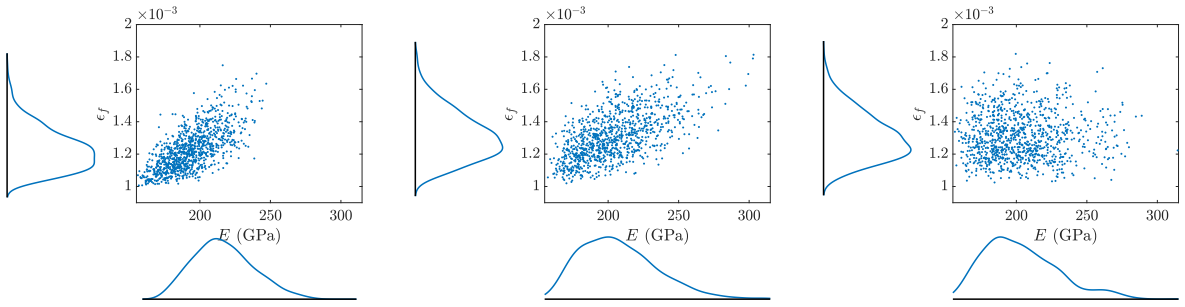

(a) True joint PDF

(b) Identified joint PDF

(c) Identified joint PDF without correlation

Figure 6: Damage: the scatter plots of the true joint PDF and the identified joint PDF with and without correlation. One can observe an increased scattering if the correlation is omitted, cf. (b) and (c).

Elastoplasticity

The same as for damage, we also assume for elastoplasticity that the true joint PDF consists of four-parameter beta distributions that are correlated via a Gaussian copula. For elastoplasticity, three univariate PDFs are required (for E, σ_0 and H) and a corresponding copula (consisting of a 3×3 covariance matrix with three independent parameters). The values selected for the true PDF are presented in Table 3.

Table 3: Elastoplasticity: the true values and the identified MAP estimates.

	True values	MAP estimates		True values	MAP estimates
α_E	4	2.1196	$\alpha_{\sigma_{y0}}$	2	2.7966
β_E	10	11.7261	$\beta_{\sigma_{y0}}$	6	5.5449
a_{1E} (GPa)	150	166.7861	$a_{1\sigma_{y0}}$ (GPa)	0.15	0.1420
a_{2E} (GPa)	300	344.4280	$a_{2\sigma_{y0}}$ (GPa)	0.5	0.4255
α_H	3	1.6400	$\rho_{E\sigma_{y0}}$	0.7071	0.6151
β_H	9	11.4085	ρ_{EH}	0.5	0.6063
a_{1H} (GPa)	30	32.8234	$\rho_{\sigma_{y0}H}$	0	0.0893
a_{2H} (GPa)	70	90.9644			

Also the same as for damage, we choose the same type of joint PDF to be identified. The priors are again chosen according to Eqs. (27) and (28), with their values shown in Table 4. We again obtain the MAP estimates by drawing 500×10^3 samples from the posterior, whilst burning the first 30% of them. Note that we again incorporate the constraint $a_1 < a_2$, but also that $\mathbf{\Gamma}_C$ must be positive semidefinite.

Table 4: Elastoplasticity: the chosen values for the parameters that define the assigned priors.

$\overline{\alpha}_E^{\text{prior}}$	2	$\overline{\alpha}_{\sigma_{y0}}^{\text{prior}}$	3
s_{α_E}	1	$s_{\alpha_{\sigma_{y0}}}$	1
$\overline{\beta}_E^{\text{prior}}$	15	$\overline{\beta}_{\sigma_{y0}}^{\text{prior}}$	7
s_{β_E}	5	$s_{\beta_{\sigma_{y0}}}$	2.3333
$\overline{a}_1{}_E^{\text{prior}}$ (GPa)	170	$\overline{a}_1{}_{\sigma_{y0}}^{\text{prior}}$ (GPa)	0.2
$s_{a_1{}_E}$ (GPa)	56.67	$s_{a_1{}_{\sigma_{y0}}}$ (GPa)	0.0667
$\overline{a}_2{}_E^{\text{prior}}$ (GPa)	270	$\overline{a}_2{}_{\sigma_{y0}}^{\text{prior}}$ (GPa)	.0.35
$s_{a_2{}_E}$ (GPa)	90	$s_{a_2{}_{\sigma_{y0}}}$ (GPa)	0.1167
$\overline{\alpha}_H^{\text{prior}}$	2	$\overline{\rho}_{E\sigma_{y0}}^{\text{prior}}$	0.9
s_{α_H}	1	$s_{\rho_{E\sigma_{y0}}}$	0.3
$\overline{\beta}_H^{\text{prior}}$	12	$\overline{\rho}_{EH}^{\text{prior}}$	0.4
s_{β_H}	4	$s_{\rho_{EH}}$	0.1
$\overline{a}_1{}_H^{\text{prior}}$ (GPa)	40	$\overline{\rho}_{\sigma_{y0}H}^{\text{prior}}$	0.1
$s_{a_1{}_H}$ (GPa)	13.3333	$s_{\rho_{\sigma_{y0}H}}$	0.0333
$\overline{a}_2{}_H^{\text{prior}}$ (GPa)	80		
$s_{a_2{}_H}$ (GPa)	26.6667		

The true joint PDF is numerically presented in Table 3 and graphically in Fig. 7 together with the identified joint PDFs with and without correlation. Similar to the results for damage, the identified joint PDF with correlation is more accurate and less wide than the identified joint PDF without correlation.

5.2. Propagating the material parameter PDFs in network models

In the previous subsection, we have clearly seen that the identified joint PDFs are relatively accurate representations of the true joint PDFs, regarding the limited number of data. We have also seen that the correlation is important to incorporate in order to achieve this accuracy. In the current subsection, we investigate how the differences between the true joint PDF and the identified joint PDF with and without correlation influences the macroscale responses of virtual fibre structures.

For the networks of type A (see Fig. 8), we investigate two configurations: one with $h = 0.1$ mm and one with $h = 0.025$ mm (where h denotes the horizontal distance between two adjacent constituents as mentioned in the previous section). Type A network with $h = 0.025$ mm thus contains 4 times more constituents than that with $h = 0.1$ mm and approximately 16 times more inter-constituent connections.

One may recall from the previous section that the networks of type B are the same as those of type A, except that the constituent length is finite and that their orientation is not the same. We investigate two different constituent lengths: one given by randomly sampling them from a uniform distribution with bounds 0.3 mm and 0.6 mm and one with bounds 1 mm and 1.5 mm. For both lengths, we also investigate different constituent densities: one given by $h = 0.1$ mm and one given by $h = 0.025$ mm. The remaining geometrical parameters for type B networks are $w_\theta = 15^\circ$ and $h_c = 0.2h$. Some typical realisations can be seen in Figs. 9 and 10.

For the geometrically completely random networks (type C), we investigate two cases. In the first case we use 2000 constituents (Fig. 11) and in the second we use 5000 constituents. In both cases the constituent lengths are randomly taken from a uniform distribution with bounds 0.5 mm and 1 mm.

For each type of network, we simulate the mechanical responses of 1000 realisations. In case of damage, the stiffness matrix may become singular during a simulation, e.g. because the crack propagates through one of the domain edges to which boundary conditions are applied. In those cases, the predicted results are ignored for the analyses below.

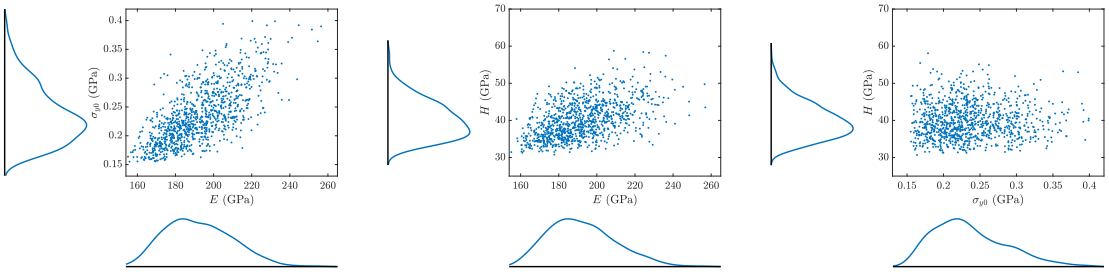

Figure 7: Elastoplasticity: three views of the scatter plots of the true joint PDF (top row) and the identified joint PDF with correlation (centre row) and without correlation (bottom row). One can observe an increased scattering if the correlation is omitted, cf. (d,e,f) and (g,h,i).

Damage

Some typical damage patterns and force-displacements curves are presented in Figs. 8 to 11. For each response, we determine the maximum force ($F_{\max}$) and the dissipated energy (η) as measures for the macroscale response of the networks.

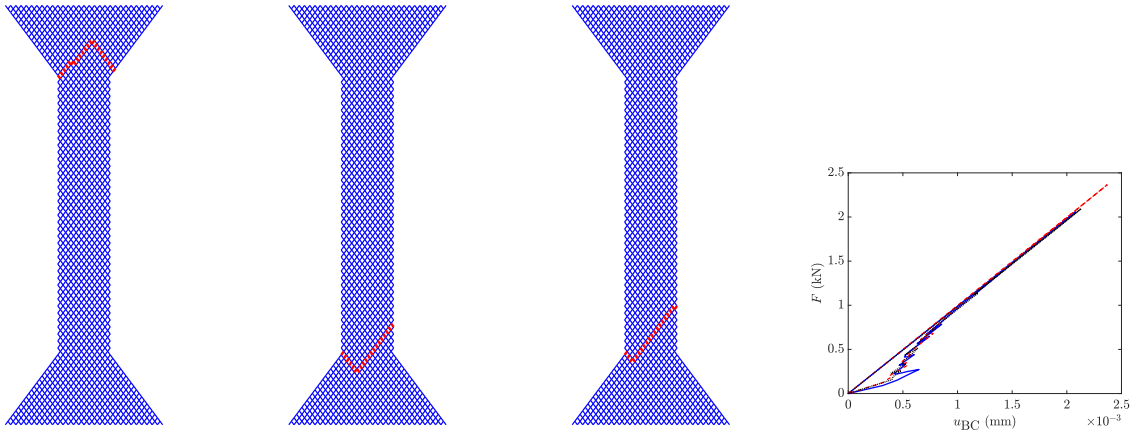

(a) (b) (c) (d)

Figure 8: Damage: some typical damage patterns for the type A networks with $h = 0.1$ mm (red: failed constituents) and some force-displacement curves.

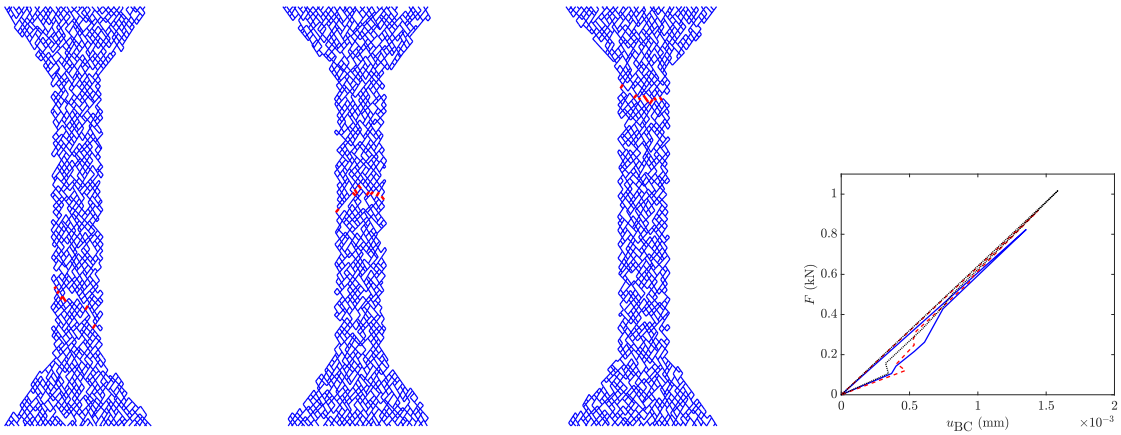

(a) (b) (c) (d)

Figure 9: Damage: some typical damage patterns for the type B networks with $h = 0.1$ mm and constituent lengths ranging between 0.3 mm and 0.6 mm (red: failed constituents), as well as some force-displacement curves.

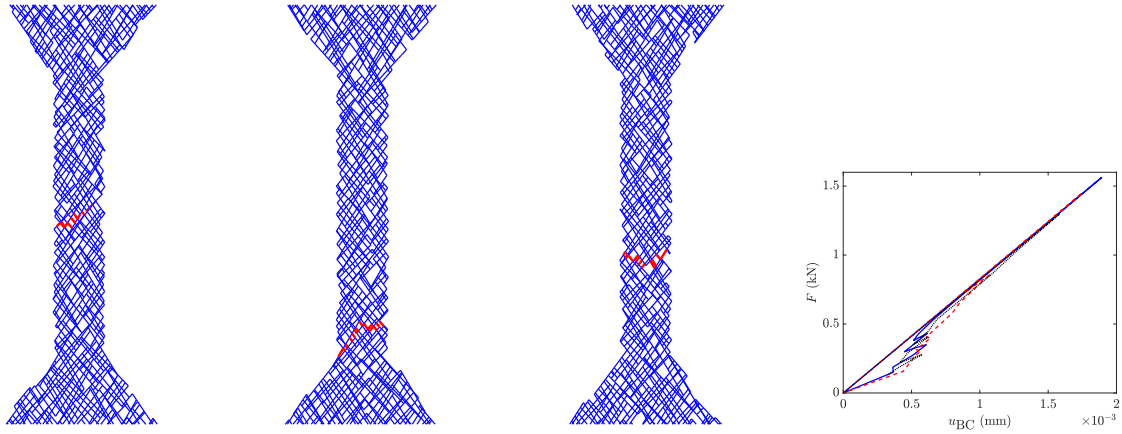

(a) (b) (c) (d)

Figure 10: Damage: some typical damage patterns for the type B networks with $h = 0.1$ mm and constituent lengths ranging between 1 mm and 1.5 mm (red: failed constituents), as well as some force-displacement curves.

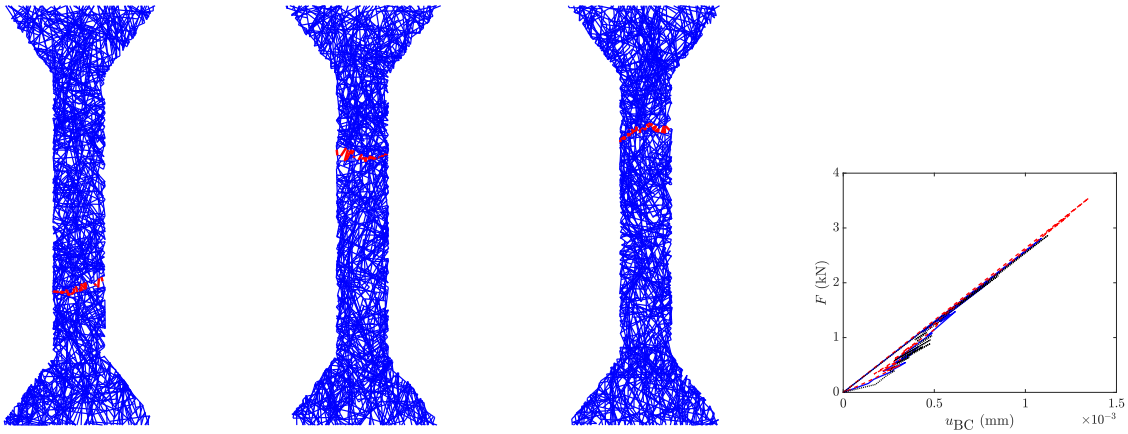

(a) (b) (c) (d)

Figure 11: Damage: some typical damage patterns for the type C networks with 2000 constituents (red: failed constituents) and some force-displacement curves.

Fig. 12 shows the scatter plot of the maximum force and dissipated energy for the type A network with $h = 0.1$ mm. The first issue to observe, which can also be observed for the type A network with $h = 0.025$ mm, is that two domains seem to be present. We characterise the first domain in the results of the true PDF roughly by $0.08 < \eta < 0.13$ mJ, whereas the second domain roughly by $0.13 < \eta < 0.25$ mJ. The difference between these domains is caused by the damage pattern. We have observed that cracked beams remain present in the narrow part of the dog-bone shaped specimens for the points in the first domain, whilst cracked beams also appear in the wider parts at the top and bottom of the dog-bone shaped specimens for points in the second domain. For the latter, longer crack lengths therefore occur, explaining the increase in dissipation.

Comparing Figs. 12(a), 12(b) and 12(c), one can see that the marginal univariate PDFs for all three cases are similar, although the ones predicted using identified marginal univariate PDFs are clearly wider. The mean values of the maximum force and dissipated energy and the Pearson correlation coefficients are presented in Table 5. It can be observed that the mean values for both the maximum force and the dissipated

energy are higher for the cases with the identified joint PDFs than for the cases with the true PDF. The difference in the results between whether or not incorporating the correlation is negligible.

Fig. 13 shows the same scatter plot, but with $h = 0.025$ mm, i.e. for an increased fibre density. The trends are similar as for the case of $h = 0.025$ mm. Even the relative difference between the means is very similar (Table 5).

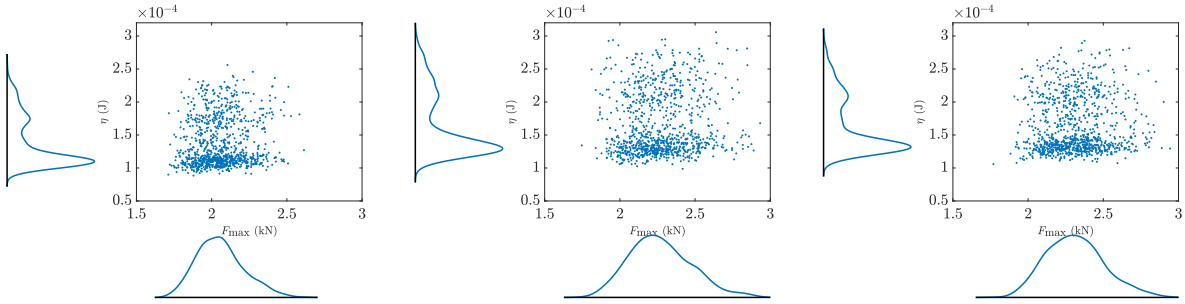

(a) True joint PDF (b) Identified joint PDF (c) Identified joint PDF without correlation

Figure 12: Damage: the scatter plots of the maximum force ($F_{\max}$) and dissipated energy (η) for the type A networks with $h = 0.1$ mm. One can see that the marginal univariate PDFs are similar in all the cases. One can also observe that the marginal univariate PDF for the dissipation consists of two domains. The first ($\eta < 0.13$ mJ) contains predictions with shorter crack paths than the second ($\eta > 0.13$ msJ), caused by crack path being present in the wide top and bottom regions of the dog-bone shaped specimens.

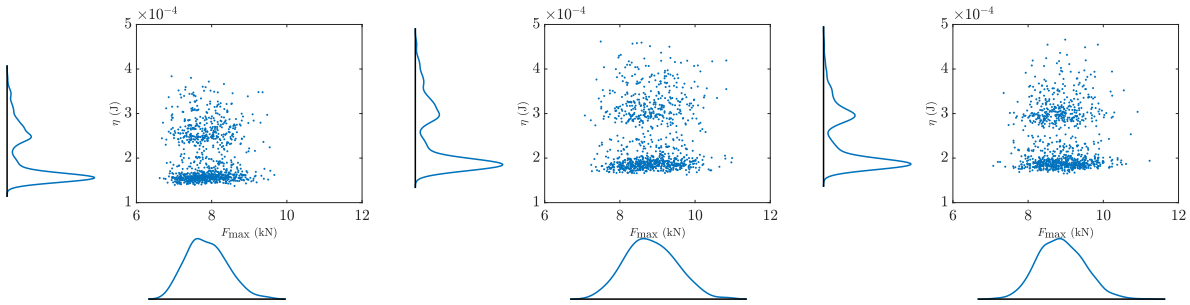

(a) True joint PDF (b) Identified joint PDF (c) Identified joint PDF without correlation

Figure 13: Damage: the scatter plots of the maximum force ($F_{\max}$) and dissipated energy (η) for the type A networks with $h = 0.025$ mm. One can see that the marginal univariate PDFs are similar in all the cases. Like the case with $h = 0.1$ mm and regardless of the used material parameter PDF, one can see that the marginal univariate PDF for the dissipation consists of two domains. This is caused by long fracture paths that propagate through the wide top and bottom regions of the dog-bone shaped specimens (see Fig. 8(a)), resulting in an increase of the dissipation.

Next, we consider type B networks with constituent lengths randomly sampled from a uniform distribution with bounds 0.3 mm and 0.6 mm. Fig. 14 presents the scattered plot of the maximum force and dissipated energy for $h = 0.1$ mm and the mean values and correlation coefficient are given in Table 6. One can see that the mean values of the maximum force and dissipated energy are higher for both cases with the identified joint PDF than for the cases with the true joint PDF. However, this is not the case for the correlation coefficient. The difference between the cases with the identified joint PDF with and without correlation is negligible.

Table 5: Damage: the mean values and Pearson correlation coefficient for the type A networks.

h (mm)	$F_{\max}^{\text{mean}}$ (kN)	η^{mean} (J)	$\rho_{F_{\max}\eta}$
True joint PDF			
0.1	2.0584	1.3703×10^{-4}	0.1067
0.025	7.8706	2.0107×10^{-4}	-0.0053
Identified joint PDF			
0.1	2.27014	1.647×10^{-4}	0.0734
0.025	8.8204	2.4216×10^{-4}	0.02069
Identified joint PDF without correlation			
0.1	2.3142	1.6342×10^{-4}	0.0402
0.025	8.8744	2.3866×10^{-4}	-5.5635×10^{-4}

If we now increase the fibre density (by setting $h = 0.025$ mm), we can see the same trend as for the type A networks (Fig. 15 and Table 6): although the mean of the maximum force and dissipated energy increase, the relative differences between the mean values of the cases with the true joint PDF and the identified joint PDFs remain similar. Increasing the constituent length ($l_{\min} = 1$ mm and $l_{\max} = 1.5$ mm) has practically no influence on the relative differences between the cases with the true PDF and the identified PDFs (Figs. 16 and 17).

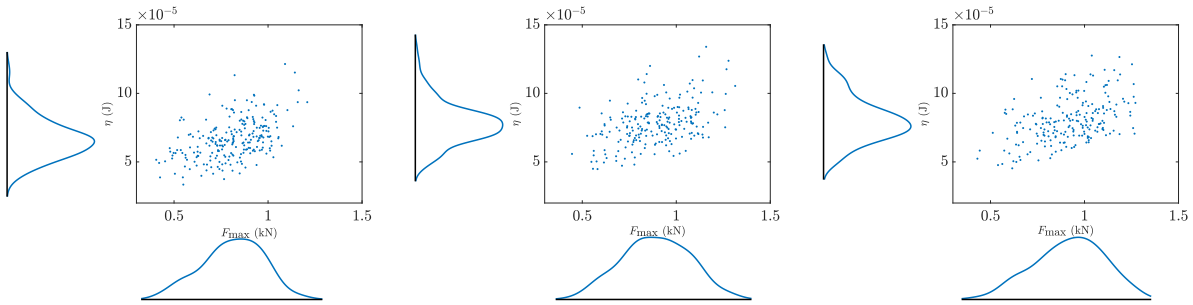

(a) True joint PDF (b) Identified joint PDF (c) Identified joint PDF without correlation

Figure 14: Damage: the scatter plots of the maximum force ($F_{\max}$) and dissipated energy (η) for the type B networks with constituent lengths randomly sampled from a uniform distribution with bounds 0.3 mm and 0.6 mm and $h = 0.1$ mm. One can observe similar trends for all cases. The means are larger for the cases with the identified PDFs than for the cases with the true PDF (also see Table 6).

Table 6: Damage: the mean values and Pearson correlation coefficient for the type B networks with constituent lengths randomly sampled from a uniform distribution with bounds 0.3 mm and 0.6 mm.

h (mm)	$F_{\max}^{\text{mean}}$ (kN)	η^{mean} (J)	$\rho_{F_{\max}\eta}$
True joint PDF			
0.1	0.8103	6.6701×10^{-5}	0.4855
0.025	6.4519	1.4362×10^{-4}	0.0931
Identified joint PDF			
0.1	0.8900	7.7875×10^{-5}	0.4582
0.025	7.2117	1.7117×10^{-4}	0.0686
Identified joint PDF without correlation			
0.1	0.9184	8.0536×10^{-5}	0.4655
0.025	7.2788	1.7187×10^{-4}	0.1187

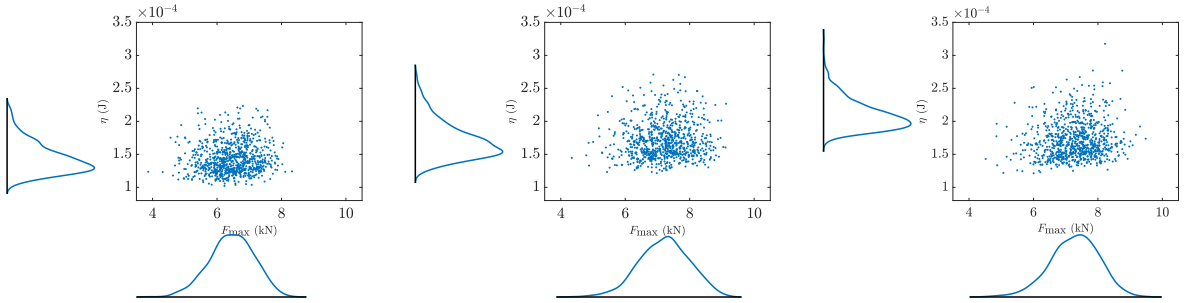

(a) True joint PDF (b) Identified joint PDF (c) Identified joint PDF without correlation

Figure 15: Damage: the scatter plots of the maximum force ($F_{\max}$) and dissipated energy (η) for the type B networks with constituent lengths randomly sampled from uniform distribution with bounds 0.3 mm and 0.6 mm and $h = 0.025$ mm. One can observe similar trends for all cases. The means are larger for the cases with the identified PDFs than for the cases with the true PDF (Table 6).

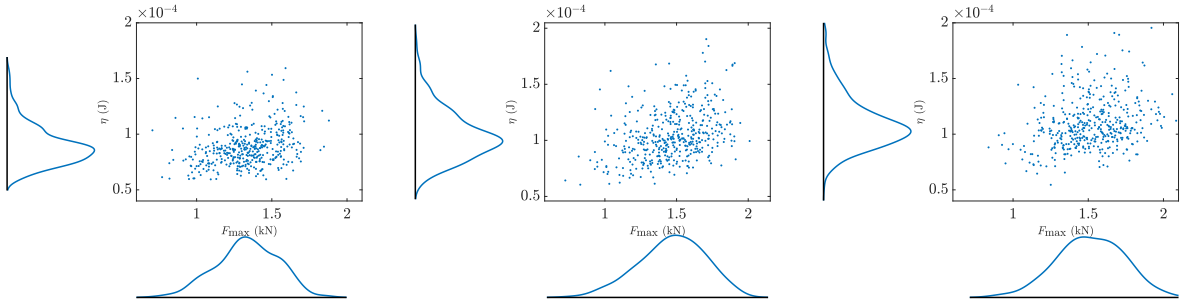

(a) True joint PDF (b) Identified joint PDF (c) Identified joint PDF without correlation

Figure 16: Damage: the scatter plots of the maximum force ($F_{\max}$) and dissipated energy (η) for the type B networks with constituent lengths randomly sampled from a uniform distribution with bounds 1 mm and 1.5 mm and $h = 0.1$ mm. One can observe similar trends for all cases. The means are larger for the cases with the identified PDFs than for the cases with the true PDF (Table 7).

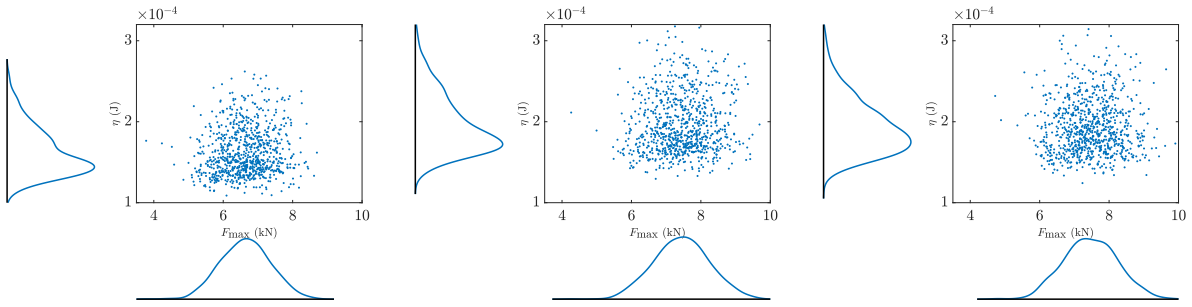

(a) True joint PDF

(b) Identified joint PDF

(c) Identified joint PDF without correlation

Figure 17: Damage: the scatter plots of the maximum force ($F_{\max}$) and dissipated energy (η) for the type B networks with constituent lengths randomly sampled from a uniform distribution with bounds 1 mm and 1.5 mm and $h = 0.025$ mm. One can observe similar trends for all cases. The means are larger for the cases with the identified PDFs than for the cases with the true PDF (Table 7).

Table 7: Damage: the mean values and Pearson correlation coefficient for the type B networks with constituent lengths randomly sampled from uniform distribution with bounds 1 mm and 1.5 mm.

h (mm)	$F_{\max}^{\text{mean}}$ (kN)	η^{mean} (J)	$\rho_{F_{\max}\eta}$
True joint PDF			
0.1	1.3353	8.9301×10^{-5}	0.2929
0.025	6.6424	1.6227×10^{-4}	0.1080
Identified joint PDF			
0.1	1.4664	1.0496×10^{-4}	0.3600
0.025	7.4416	1.9584×10^{-4}	0.0737
Identified joint PDF without correlation			
0.1	1.5131	1.0977×10^{-4}	0.2430
0.025	7.4673	1.9346×10^{-4}	0.0192

Finally, we consider the results for the type C networks. Again, the same trends can be observed: increasing the fibre density causes a shift of the PDFs, the PDFs of the cases with the identified PDFs have larger means than those of the cases with the true PDF, but the relative differences between the means is again roughly 10%. Incorporating the correlation has a negligible effect on the results.

Table 8: Damage: the mean values and Pearson correlation coefficient for the type C networks.

Number of constituents	$F_{\max}^{\text{mean}}$ (kN)	η^{mean} (J)	$\rho_{F_{\max}\eta}$
True joint PDF			
2000	3.2110	1.1724×10^{-4}	0.2274
5000	11.2996	1.6765×10^{-4}	0.0775
Identified joint PDF			
2000	3.6055	1.4084×10^{-4}	0.2416
5000	12.7403	2.0117×10^{-4}	0.0498
Identified joint PDF without correlation			
2000	3.6680	1.3764×10^{-4}	0.2374
5000	12.7334	1.9868×10^{-4}	0.0215

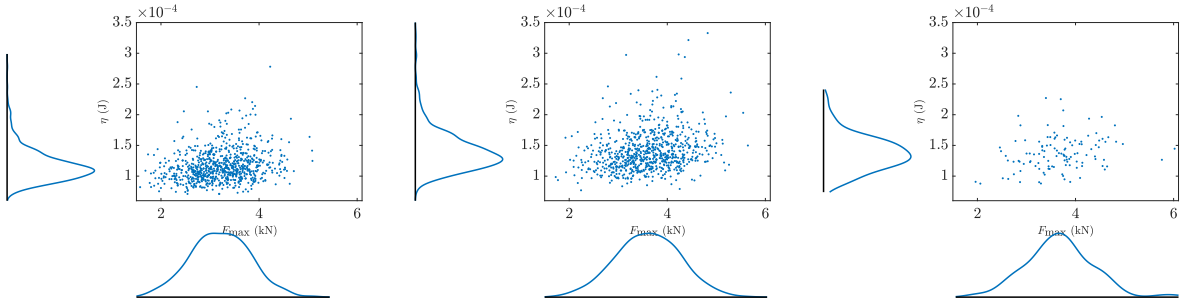

(a) True joint PDF (b) Identified joint PDF (c) Identified joint PDF without correlation

Figure 18: Damage: the scatter plots of the maximum force ($F_{\max}$) and dissipated energy (η) for the type C networks with 2000 constituents. The mean values of the maximum force, dissipated energy, as well as the correlation coefficient are shown in Table 8.

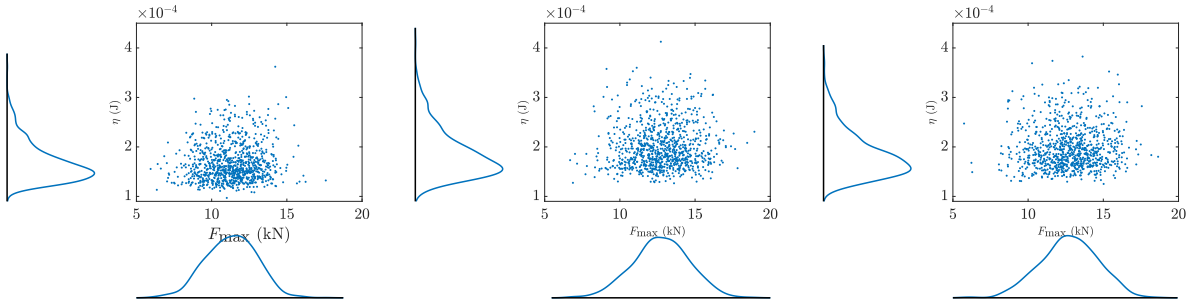

(a) True joint PDF (b) Identified joint PDF (c) Identified joint PDF without correlation

Figure 19: Damage: the scatter plots of the maximum force ($F_{\max}$) and dissipated energy (η) for the type C networks with 5000 constituents. The mean values of the maximum force, dissipated energy, as well as the correlation coefficient are shown in Table 8.

Elastoplasticity

Some typical results of individual simulations for elastoplasticity are shown in Figs. 20 to 23. For the statistical analyses below, we describe the predicted force-displacement responses using the typical 1D expression of isotropic elastoplasticity with linear hardening for monotonically increasing, uniaxial tension, in which reaction force F is a function of prescribed displacement u_{BC} (see Fig. 2) as follows:

$$F = \begin{cases} k_E u_{\mathrm{BC}} & \text{if } u_{\mathrm{BC}} < \frac{F_{y0}}{k_E} \\ F_{y0} + \frac{k_E k_P}{k_E + k_P}(u_{\mathrm{BC}} - \frac{F_{y0}}{k_E}) & \text{if } \epsilon \geq \frac{F_{y0}}{k_E} \end{cases}, \tag{29}$$

where k_E, F_{y0} and k_P denote the system's equivalent elastic stiffness, initial yield force and hardening stiffness, respectively.

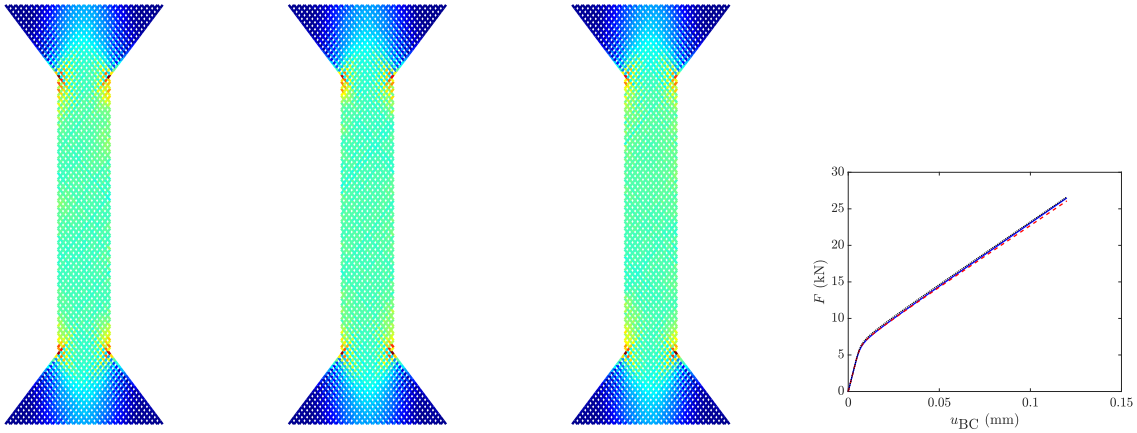

(a) (b) (c) (d)

Figure 20: Elastoplasticity: some typical patterns of the maximum cumulative plastic strain per beam element for the type A networks with $h = 0.1$ mm (blue: no cumulative plastic strain, red: maximum cumulative plastic strain), as well as some force-displacement curves.

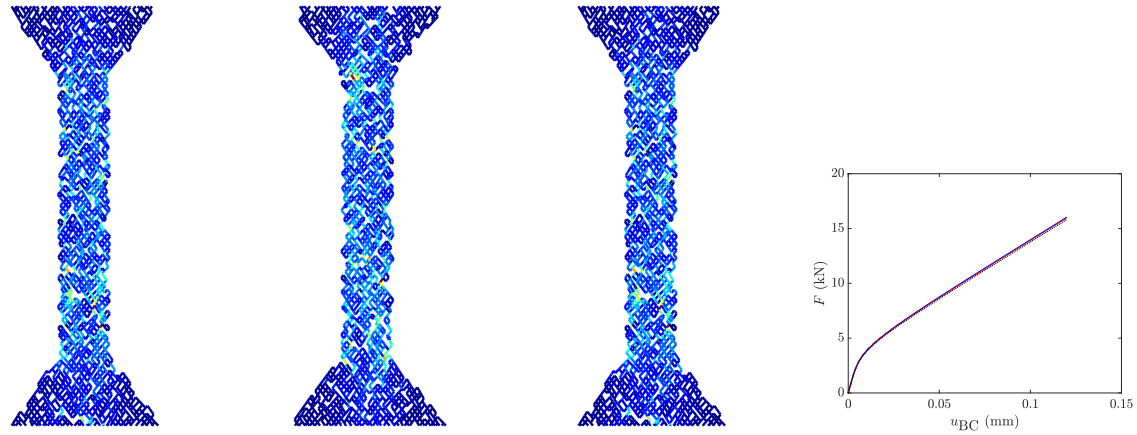

(a) (b) (c) (d)

Figure 21: Elastoplasticity: some typical patterns of the maximum cumulative plastic strain per beam element for the type B networks with $h = 0.1$ mm and constituent lengths ranging between 0.3 mm and 0.6 mm (blue: no cumulative plastic strain, red: maximum cumulative plastic strain), as well as some force-displacement curves.

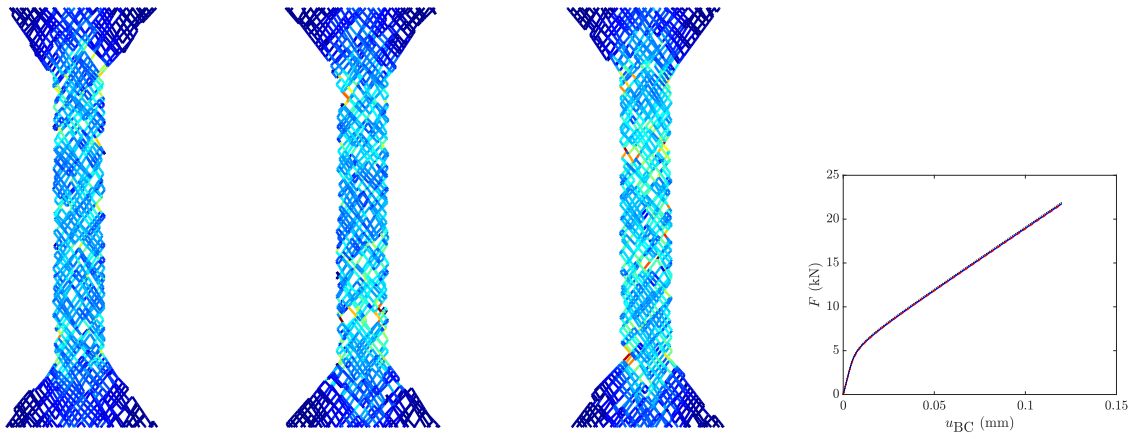

(a) (b) (c) (d)

Figure 22: Elastoplasticity: some typical patterns of the maximum cumulative plastic strain per beam element for the type B networks with $h = 0.1$ mm and constituent lengths ranging between 1 mm and 1.5 mm (blue: no cumulative plastic strain, red: maximum cumulative plastic strain), as well as some force-displacement curves.

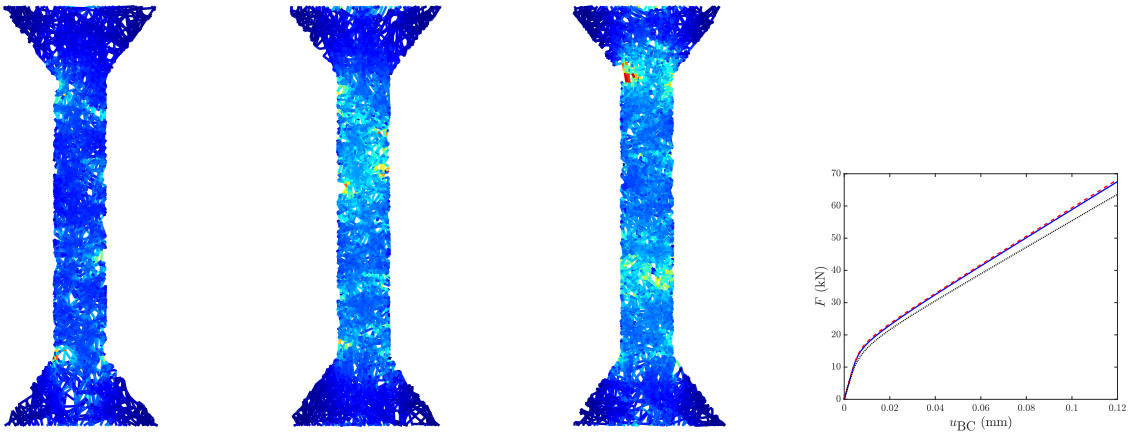

(a) (b) (c) (d)

Figure 23: Elastoplasticity: some typical patterns of the maximum cumulative plastic strain per beam element for the type C networks with 2000 constituents (blue: no cumulative plastic strain, red: maximum cumulative plastic strain), as well as some force-displacement curves.

We start again by discussing the scatter plots for the networks of type A with $h = 0.1$ mm, which are presented on three different planes in Fig. 24. The mean values of k_E and k_P are again somewhat larger for the cases with the identified PDFs than for the cases with the true PDF (Table 9), but a substantial difference can now be observed for the cases with the identified PDF with and without correlation: the PDF predicted with correlation is substantially closer to the PDF predicted with the true material parameter PDF than the PDF predicted without correlation.

If we increase the constituent density by reducing $h = 0.1$ mm to $h = 0.025$ mm, we see similar trends (Fig. 25 and Table 9). The mean values of k_E and k_P are again approximately 0.5% larger for the cases with the identified PDFs than for the cases with the true PDF and the correlation is significantly better predicted by the cases with the identified PDF with correlation than by the cases with the identified PDF without correlation.

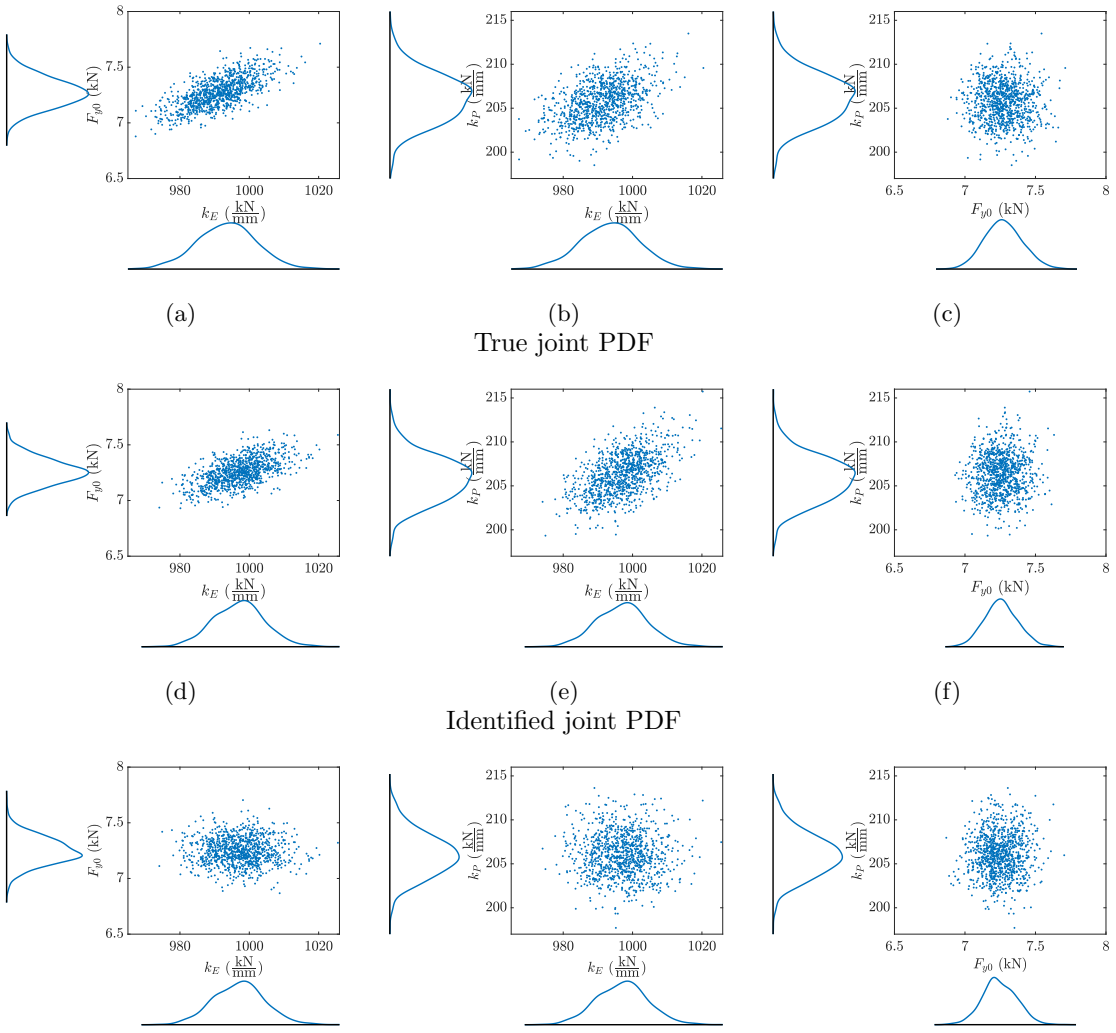

Figure 24: Elastoplasticity: the scatter plots of the systems' equivalent elastic stiffness (k_E), initial yield force (F_{y0}) and plastic stiffness (k_P) for the type A networks with $h = 0.1$ mm. Comparing (a), (d) and (g) and (b), (e) and (h) shows that the correlation between system parameters is substantially better predicted by the cases with the identified PDF with correlation than by the cases with the identified PDF without correlation.

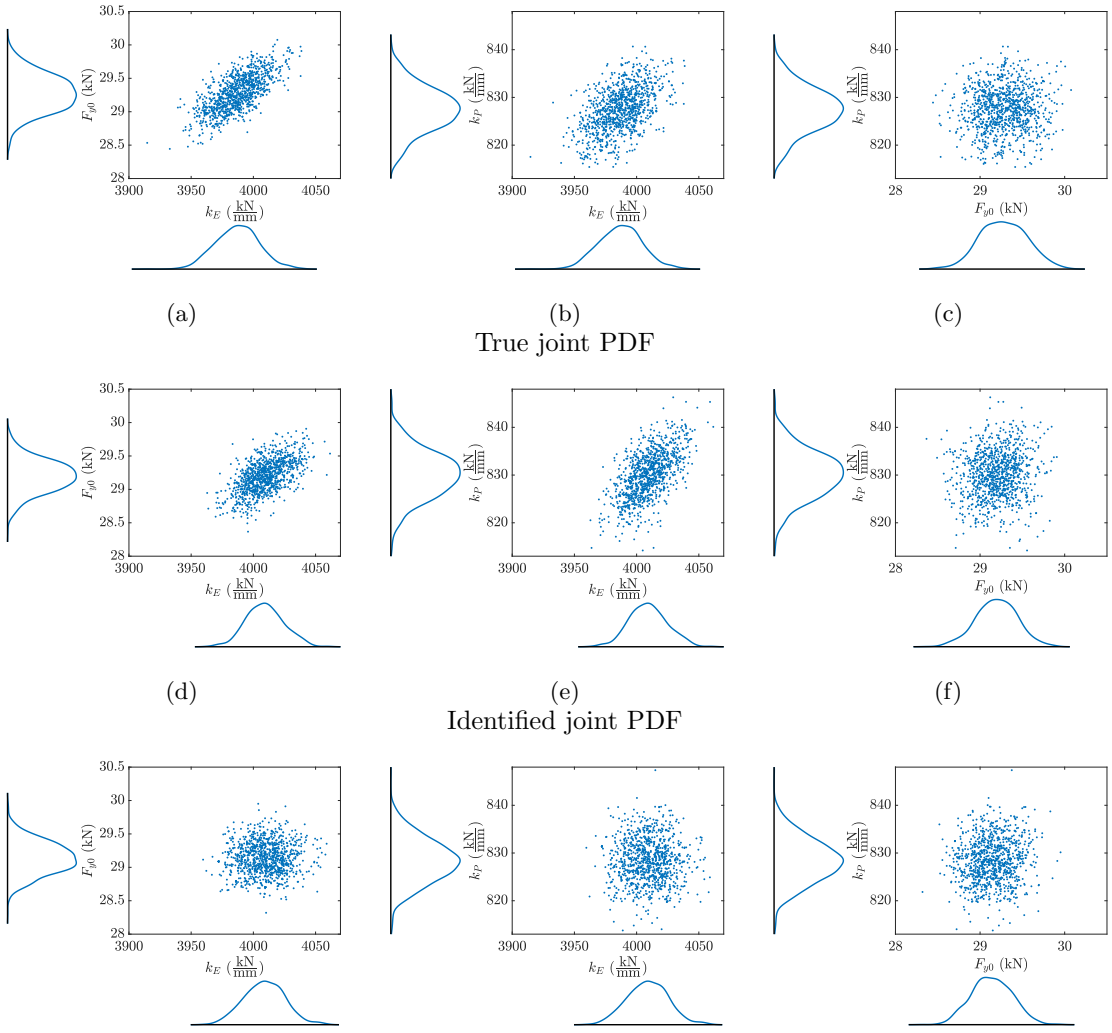

Figure 25: Elastoplasticity: the scatter plots of the systems' equivalent elastic stiffness (k_E), initial yield force (F_{y0}) and plastic stiffness (k_P) for the type A networks with $h = 0.025$ mm. Similar as for the case with $h = 0.1$, the correlation between the system parameters is substantially better predicted by the cases with the identified PDF with correlation than by the cases with the identified PDF without correlation.

Table 9: Elastoplasticity: the mean values and Pearson correlation coefficients for the type A networks.

h (mm)	k_E^{mean} ($\frac{\text{kN}}{\text{mm}}$)	F_{y0}^{mean} (kN)	k_P^{mean} ($\frac{\text{kN}}{\text{mm}}$)	$\rho_{k_E F_{y0}}$	$\rho_{k_E k_P}$	$\rho_{F_{y0} k_P}$
True joint PDF						
0.1	991.1905	7.2735	205.7121	0.6790	0.4605	-0.0257
0.025	3987.025	29.2798	827.4717	0.7057	0.5077	0.0502
Identified joint PDF						
0.1	997.0578	7.2563	206.3549	0.5805	0.5535	0.0605
0.025	4009.4294	29.1966	830.0712	0.5793	0.6074	0.1056
Identified joint PDF without correlation						
0.1	997.0578	7.2463	206.0329	-0.0228	-0.0249	0.0471
0.025	4008.8975	29.1396	828.4127	0.0439	0.0046	0.0948

If we now increase the geometrical randomness by considering the networks of type B characterised by $l_{\min} = 0.3$ mm, $l_{\max} = 0.3$ mm and $h = 0.1$ mm, we see that the correlation increases substantially (Fig. 26 and Table 10). Consequently, incorporating the correlation in the identified PDF seems of less influence than if type A networks are considered. We nevertheless still observe that the PDF predicted with the identified PDF with correlation is closer to the PDF predicted with the true PDF than the PDF predicted with the identified PDF without correlation. Increasing the fibre density (by setting $h = 0.025$ mm, instead of $h = 0.1$ mm) makes this difference grow (see Fig. 27 and Table 10).

Table 10: Elastoplasticity: the mean values and Pearson correlation coefficients for the type B networks with constituent lengths randomly sampled from a uniform distribution with bounds 0.3 mm and 0.6 mm.

h (mm)	k_E^{mean} ($\frac{\text{kN}}{\text{mm}}$)	F_{y0}^{mean} (kN)	k_P^{mean} ($\frac{\text{kN}}{\text{mm}}$)	$\rho_{k_E F_{y0}}$	$\rho_{k_E k_P}$	$\rho_{F_{y0} k_P}$
True joint PDF						
0.1	602.0250	4.4260	125.3475	0.9522	0.9773	0.9008
0.025	3688.1158	27.0729	765.4818	0.6984	0.6128	0.1191
Identified joint PDF						
0.1	605.7327	4.4164	125.7086	0.9593	0.9593	0.9251
0.025	3708.7848	26.9940	768.1752	0.6410	0.7212	0.2746
Identified joint PDF without correlation						
0.1	605.7224	4.4094	125.5335	0.9337	0.9572	0.9278
0.025	3709.4773	26.9600	766.6929	0.1778	0.3156	0.0694

If we now increase the length of the constituents by setting $l_{\min} = 1$ mm and $l_{\max} = 1.5$ mm, we also see that the correlation between the systems parameters is better captured if the correlation is incorporated in the identified PDF (see Fig. 28 and Table 11). We also see that if we increase the constituent density (by reducing $h = 0.1$ mm to $h = 0.025$ mm), the importance of incorporating the correlation increases (see Fig. 29 and Table 11). We can also conclude by comparing these results with the ones in which the constituent lengths is bound by $l_{\min} = 0.3$ mm and $l_{\max} = 0.6$ mm, that a reduction of the constituent length leads to an increase of the intrinsic correlation between system parameters (regardless of the material parameter PDF used).

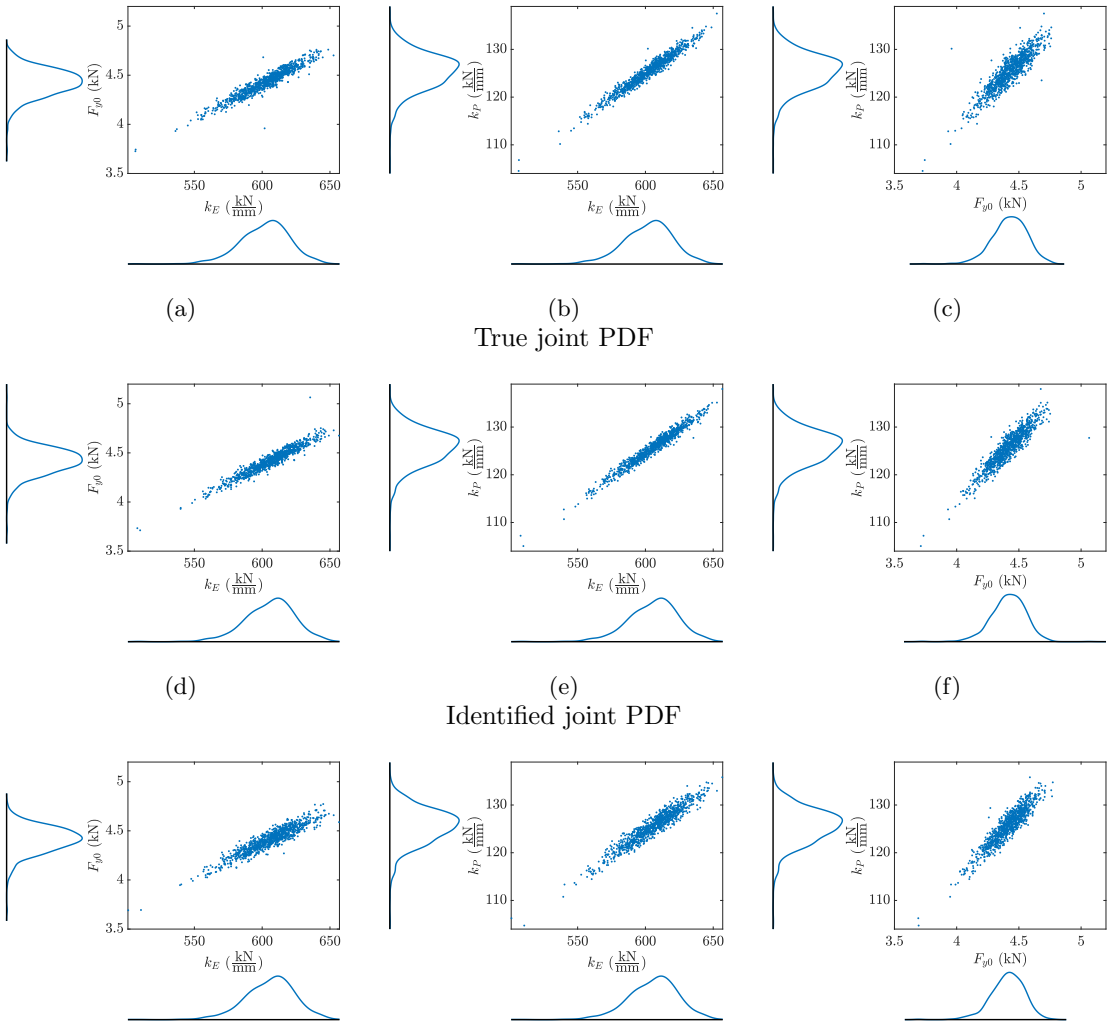

Figure 26: Elastoplasticity: the scatter plots of the systems' equivalent elastic stiffness (k_E), initial yield force (F_{y0}) and plastic stiffness (k_P) for the type B networks with constituent lengths randomly sampled from a uniform distribution with bounds 0.3 mm and 0.6 mm and $h = 0.1$ mm. The results show that the effect of the correlation between the material parameters is smaller than for the type A networks, but remains to be present. The numerical values are presented in Table 10.

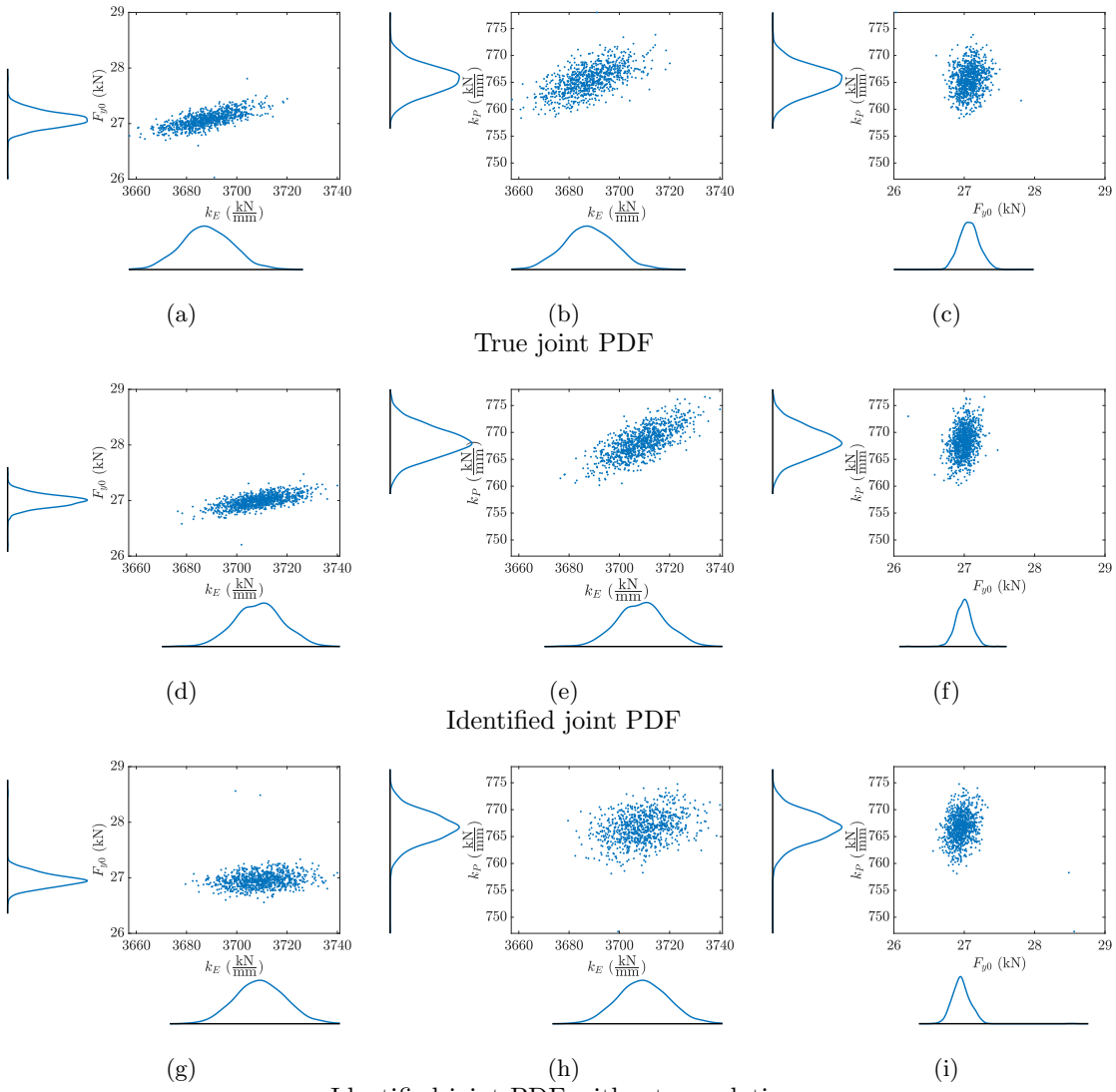

Figure 27: Elastoplasticity: the scatter plots of the systems' equivalent elastic stiffness (k_E), initial yield force (F_{y0}) and plastic stiffness (k_P) for the type B networks with constituent lengths randomly sampled from a uniform distribution with bounds 0.3 mm and 0.6 mm and $h = 0.025$ mm. The influence of the correlation has increased due to the increased constituent density (cf. Fig. 26). The corresponding numerical values are given in Table 10.

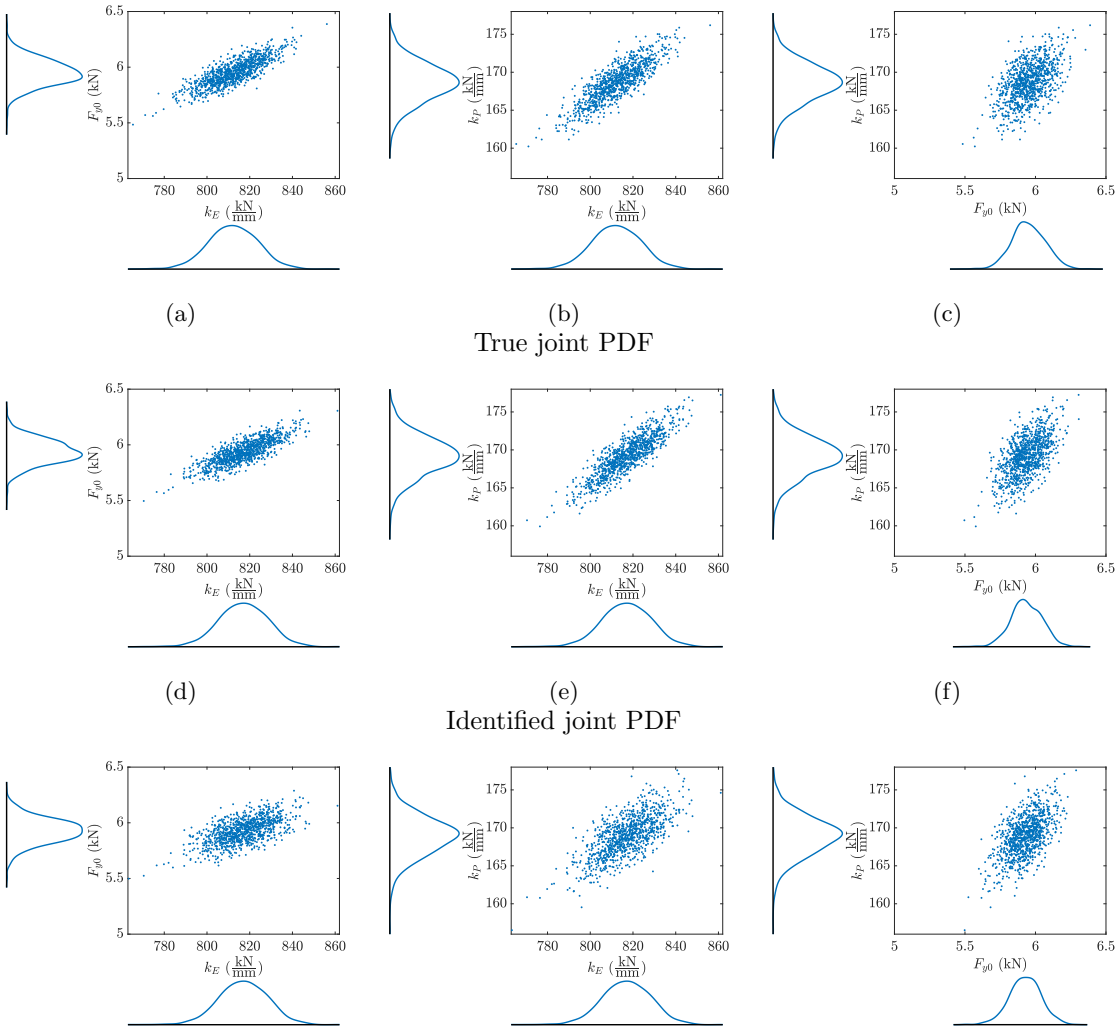

Figure 28: Elastoplasticity: the scatter plots of the systems' equivalent elastic stiffness (k_E), initial yield force (F_{y0}) and plastic stiffness (k_P) for the type B networks with constituent lengths randomly sampled from uniform distribution with bounds 1 mm and 1.5 mm and $h = 0.1$ mm. The results show that the influence of the correlation is important to incorporate. The numerical values are presented in Table 11.

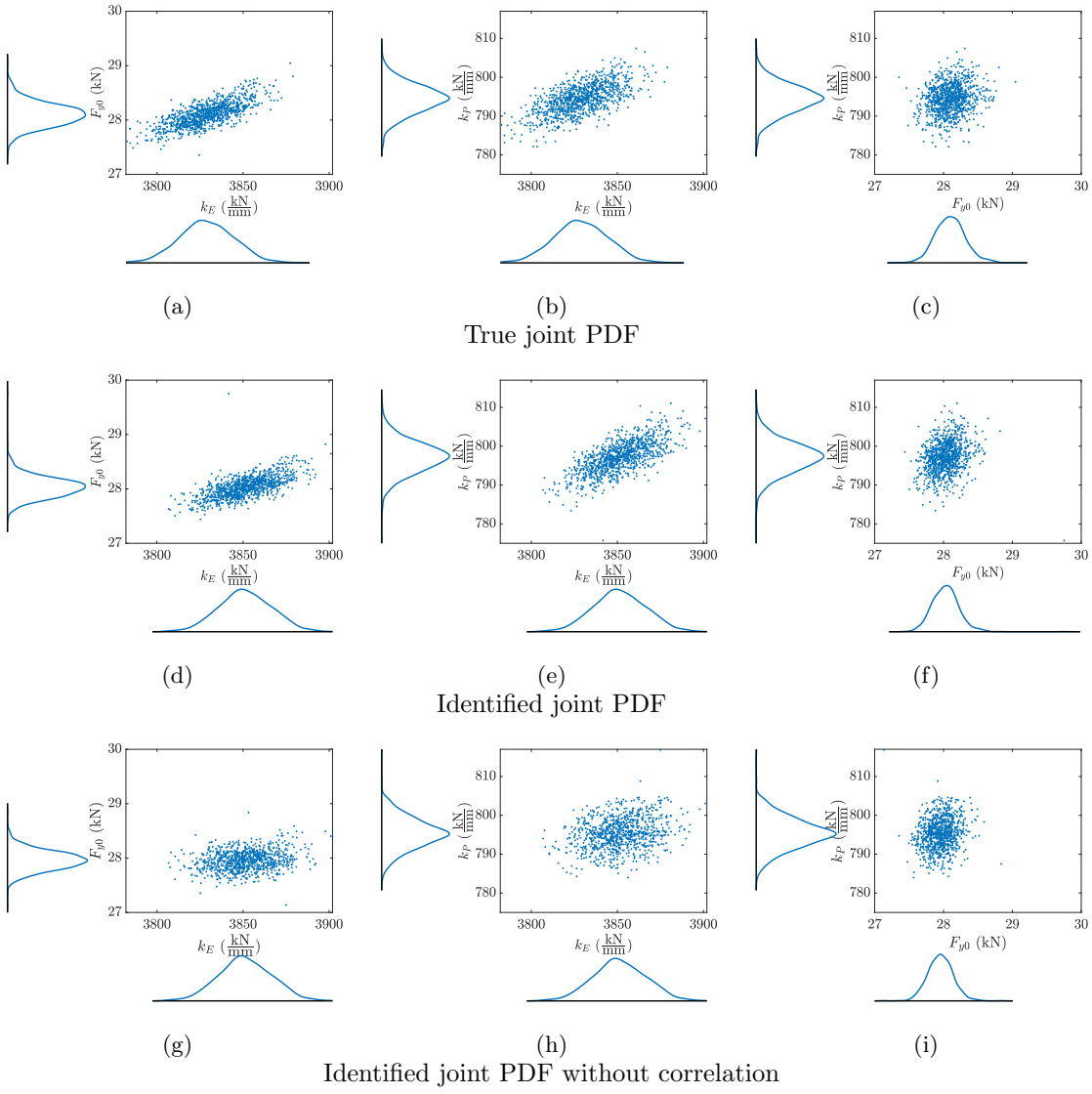

Figure 29: Elastoplasticity: the scatter plots of the systems' equivalent elastic stiffness (k_E), initial yield force (F_{y0}) and plastic stiffness (k_P) for the type B networks with constituent lengths randomly drawn from a uniform distribution with bounds 1 mm and 1.5 mm and $h = 0.025$ mm. The results show that the influence of the correlation is more important to incorporate due to the increased fibre density (cf. Fig. 28). The numerical values are presented in Table 11.

Finally, we show the results for the type C networks (Figs. 30 and 31 and Table 12). We see that the intrinsic correlation between the system's parameters (regardless of the material parameter PDF used) becomes even more pronounced than was the case for the type B networks. Apparently, this is caused by the increased geometrical randomness. Consequently, the influence of incorporating the correlation in the identified PDF becomes less important, but the cases with the identified PDF with correlation still outperform those with the identified PDF without correlation.

Table 11: Elastoplasticity: the mean values and Pearson correlation coefficients for the type B networks with constituent lengths randomly sampled from a uniform distribution with bounds 1 mm and 1.5 mm.

h (mm)	k_E^{mean} ($\frac{\text{kN}}{\text{mm}}$)	F_{y0}^{mean} (kN)	k_P^{mean} ($\frac{\text{kN}}{\text{mm}}$)	$\rho_{k_E F_{y0}}$	$\rho_{k_E k_P}$	$\rho_{F_{y0} k_P}$
True joint PDF						
0.1	812.2191	5.9523	168.6532	0.8241	0.8488	0.5362
0.025	3828.9229	28.1010	794.4644	0.7389	0.6384	0.1997
Identified joint PDF						
0.1	817.0609	5.9371	169.2043	0.8165	0.8696	0.6005
0.025	3851.4226	28.0314	797.1486	0.6566	0.6957	0.2260
Identified joint PDF without correlation						
0.1	816.9840	5.9275	168.9104	0.6189	0.7018	0.5796
0.025	3851.4167	27.9573	795.3540	0.2157	0.2694	0.1635

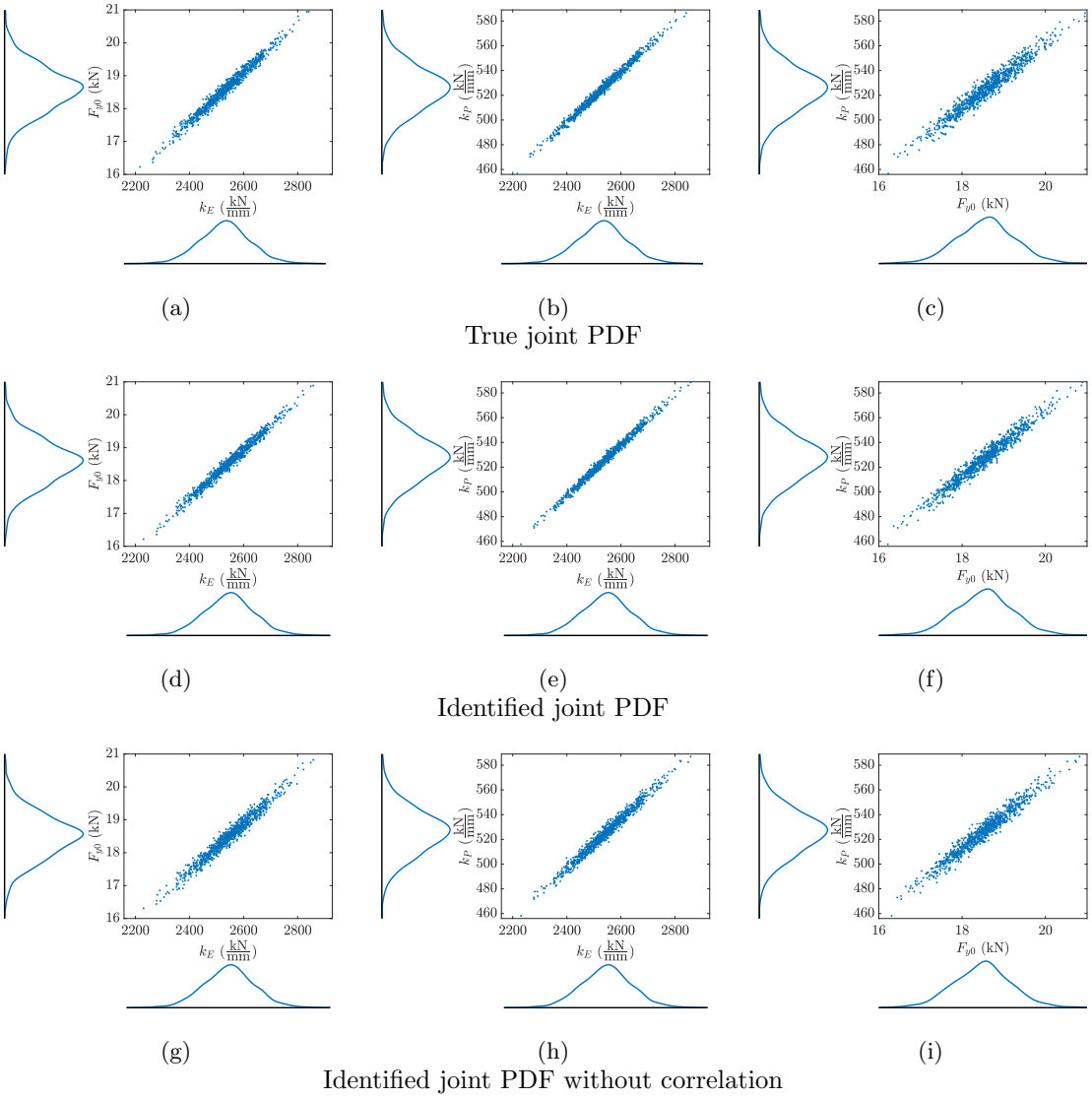

Figure 30: Elastoplasticity: the scatter plots of the systems' equivalent elastic stiffness (k_E), initial yield force (F_{y0}) and plastic stiffness (k_P) for the type C networks with 2000 constituents. Due to the increased geometrical randomness relative to the type B networks, the correlation is also captured by the cases with the identified PDF without correlation, although they are still outperformed by the cases with the identified PDF with correlation. The corresponding numerical values are given in Table 12.

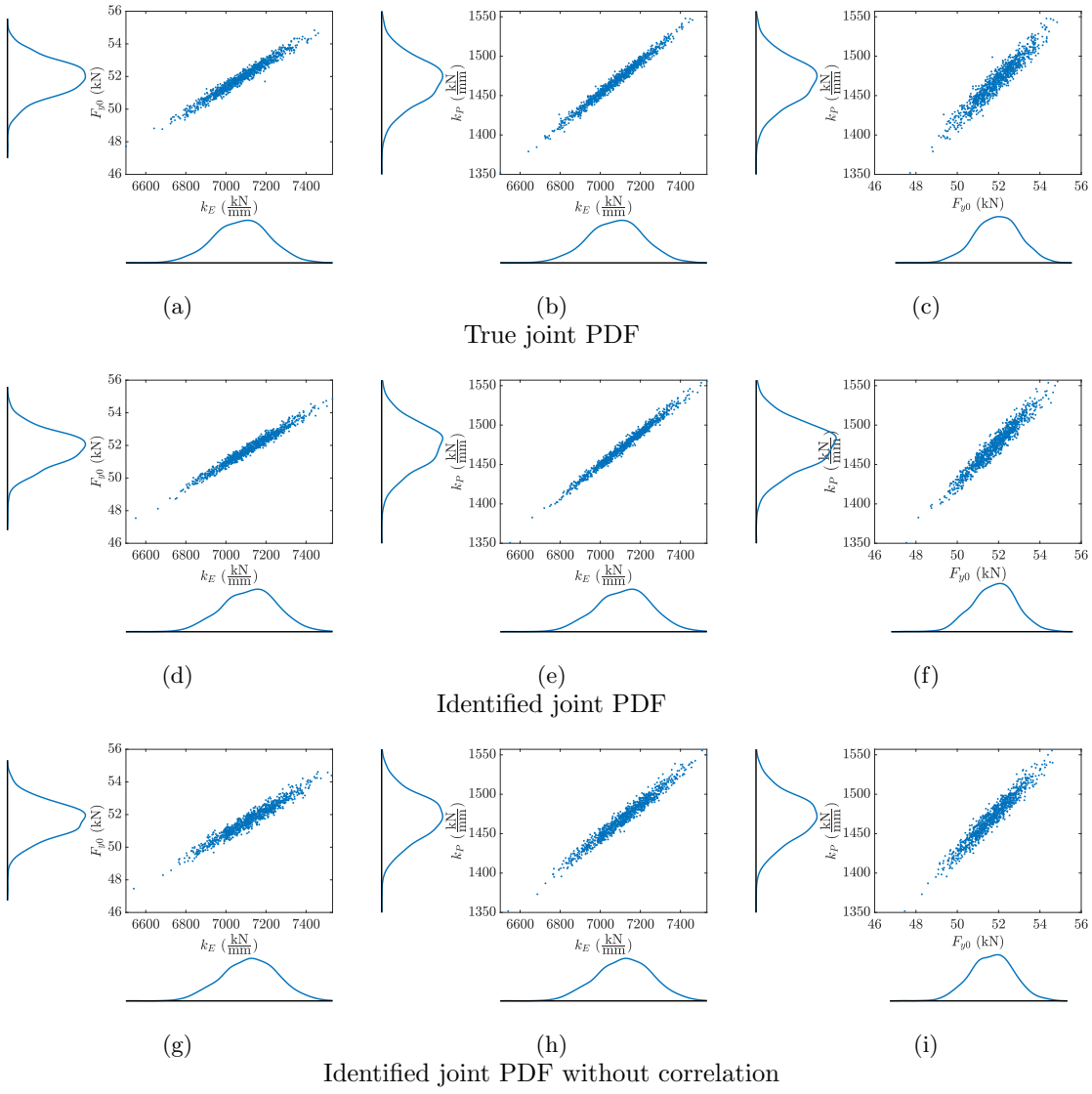

Figure 31: Elastoplasticity: the scatter plots of the systems' equivalent elastic stiffness (k_E), initial yield force (F_{y0}) and plastic stiffness (k_P) for the type C networks with 5000 constituents. Due to the increased geometrical randomness relative to the type B networks, the correlation is also captured by the cases with the identified PDF without correlation, although they are still outperformed by the cases with the identified PDF with correlation. The corresponding numerical values are given in Table 12.

5.3. Different marginal univariate PDFs

In the previous subsections the marginal univariate PDFs used to generate observations, were the same as the ones we tried to identify. Although this is a reasonable choice to illustrate the theoretical accuracy of the identification approach, in reality the type of marginal univariate PDFs are not known in advance. The objective of this subsection is to present indicative results if the marginal univariate PDFs used to generate observations are not the same as those that are to be identified. For this purpose we take the same observations from the previous subsection (which were generated with univariate beta distributions and Gaussian copulas), but now we try to model them with truncated Gaussian distribution and Gaussian copula (i.e. we try to identify univariate truncated Gaussian distributions which are coupled with a Gaussian copula). The Gaussian distribution is chosen because it is often used to model natural events. It however

Table 12: Elastoplasticity: the mean values and Pearson correlation coefficients for the type C networks.

Number of constituents	k_E^{mean} ($\frac{\text{kN}}{\text{mm}}$)	F_{y0}^{mean} (kN)	k_P^{mean} ($\frac{\text{kN}}{\text{mm}}$)	$\rho_{k_E F_{y0}}$	$\rho_{k_E k_P}$	$\rho_{F_{y0} k_P}$
True joint PDF						
2000	2531.535	18.5793	525.0600	0.9879	0.9936	0.9726
5000	7077.5611	51.9244	1468.4445	0.9824	0.9908	0.9587
Identified joint PDF						
2000	2546.6575	18.5359	526.9446	0.9897	0.9943	0.9783
5000	7118.7663	51.7978	1473.4988	0.9857	0.9926	0.9700
Identified joint PDF without correlation						
2000	2546.6575	18.4928	525.7414	0.9806	0.9882	0.9763
5000	7118.3975	51.6759	1470.2447	0.9730	0.9834	0.9683

does not have bounds (i.e. it is defined in $\mathbb{R}$) and we need to truncate it so that physical criteria (e.g. the Young's modulus must be positive) are not violated. The system macroscale behaviour is studied for both damage and elastoplasticty for the type A networks (see Fig. 3) with $h = 0.1$ mm. The type A networks with $h = 0.1$ mm are chosen because as we have seen before, the responses of these networks are most influenced by the accuracy of the identified PDF parameter values.

The univariate truncated Gaussian distribution is formulated as follows:

$$\pi_{\text{uni}i}(p_i|\mathbf{p}_{i\text{PDF}}) = \frac{\frac{1}{s_i^*}\phi\big(\frac{p_i-\mu_i}{s_i^*}\big)}{\Phi\big(\frac{a_{2i}-\mu_i}{s_i^*}\big) - \Phi\big(\frac{a_{1i}-\mu_i}{s_i^*}\big)}, \tag{30}$$

where p_i denotes the i^{th} type of parameters (i.e. E and ϵ_f for damage and E, σ_{y0} and H for elastoplasticity), μ_i and s_i^* denote the parameters of the truncated Gaussian distribution (they are the mean and standard deviation of the corresponding Gaussian distribution, i.e. $N(\mu_i, {s^*}_i^2)$), $\phi(\tilde{p})$ denotes the standard Gaussian PDF (i.e. $\frac{1}{\sqrt{2\pi}}\exp\big(-\frac{\tilde{p}^2}{2}\big)$), $\Phi(\tilde{p})$ denotes the standard Gaussian CDF and a_{1i} and a_{2i} the lower and upper bounds, respectively.

Now we can use the scheme in Section 3 to identify the marginal univariate PDFs' parameters and copula parameters. Furthermore, we again set the priors in the form of Eqs. (27) and (28). Tables 13 and 14 show the selected mean an standard deviation damage and elastoplasticity, respectively. Note that the values for $\overline{\mu}^{\text{prior}}$ and $\overline{s^*}^{\text{prior}}$ are chosen based on the mean values and standard deviations of our observations. Furthermore, the corresponding standard deviations are chosen to be relatively wide, as to not exclude any plausible values.

Table 13: Damage: the parameters that define the assigned priors.

$\overline{\mu}_E^{\text{prior}}$ (GPa)	200	$\overline{\mu}_{\epsilon_f}^{\text{prior}}$	0.0013	$\overline{\rho}_{E\epsilon_f}^{\text{prior}}$	0.9
s_{μ_E} (GPa)	66.67	$s_{\mu_{\epsilon_f}}$	4.3333×10^{-4}	$s_{\rho_{E\epsilon_f}}$	0.3
$\overline{s^*}_E^{\text{prior}}$ (GPa)	30	$\overline{s^*}_{\epsilon_f}^{\text{prior}}$	1.5315×10^{-4}		
$s_{s_E^*}$ (GPa)	10	$s_{s^*_{\epsilon_f}}$	5.105×10^{-5}		
$\overline{a}_{1E}^{\text{prior}}$ (GPa)	170	$\overline{a}_{1\epsilon_f}^{\text{prior}}$	0.0008		
$s_{a_{1E}}$ (GPa)	56.67	$s_{a_{1\epsilon_f}}$	2.6667×10^{-4}		
$\overline{a}_{2E}^{\text{prior}}$ (GPa)	270	$\overline{a}_{2\epsilon_f}^{\text{prior}}$	0.0021		
$s_{a_{2E}}$ (GPa)	90	$s_{a_{2\epsilon_f}}$	7×10^{-4}		

Table 14: Elastoplasticity: the parameters that define the assigned priors.

$\overline{\mu}_E^{\text{prior}}$ (GPa)	200	$\overline{\mu}_{\sigma_{y0}}^{\text{prior}}$ (GPa)	0.25
s_{μ_E} (GPa)	66.67	$s_{\mu_{\sigma_{y0}}}$ (GPa)	0.0833
$\overline{s^*}_E^{\text{prior}}$ (GPa)	30	$\overline{s^*}_{\sigma_{y0}}^{\text{prior}}$ (GPa)	0.05
$s_{s_E^*}$ (GPa)	10	$s_{s^*_{\sigma_{y0}}}$ (GPa)	0.0167
$\overline{a}_1{}_E^{\text{prior}}$ (GPa)	170	$\overline{a}_1{}_{\sigma_{y0}}^{\text{prior}}$ (GPa)	0.2
$s_{a_1{}_E}$ (GPa)	56.67	$s_{a_1{}_{\sigma_{y0}}}$ (GPa)	0.0667
$\overline{a}_2{}_E^{\text{prior}}$ (GPa)	270	$\overline{a}_2{}_{\sigma_{y0}}^{\text{prior}}$ (GPa)	0.35
$s_{a_2{}_E}$ (GPa)	90	$s_{a_2{}_{\sigma_{y0}}}$ (GPa)	0.1167
$\overline{\mu}_H^{\text{prior}}$ (GPa)	40	$\overline{\rho}_{E\sigma_{y0}}^{\text{prior}}$	0.9
s_{μ_H} (GPa)	13.3333	$s_{\rho_{E\sigma_{y0}}}$	0.3
$\overline{s^*}_H^{\text{prior}}$ (GPa)	6	$\overline{\rho}_{EH}^{\text{prior}}$	0.4
$s_{s_H^*}$ (GPa)	2	$s_{\rho_{EH}}$	0.1
$\overline{a}_1{}_H^{\text{prior}}$ (GPa)	40	$\overline{\rho}_{\sigma_{y0}H}^{\text{prior}}$	0.1
$s_{a_1{}_H}$ (GPa)	13.3333	$s_{\rho_{\sigma_{y0}H}}$	0.0333
$\overline{a}_2{}_H^{\text{prior}}$ (GPa)	80		
$s_{a_2{}_H}$ (GPa)	26.6667		

Similarly as in the previous subsections, we use the adaptive Metropolis algorithm to draw samples from the posteriors and approximate the statistical summaries. The number of samples drawn for each identification process is 500×10^3 whilst we burn the first 30%. Furthermore, the constraint $a_1 < a_2$ is imposed in the sampling process. Tables 15 and 16 show the point estimates approximated by the drawn samples for both damage and elastoplasticity. In addition, the true values of the correlation parameters and the identified correlation values when the marginal univariate PDFs are the same as the true ones are presented. Note that in these tables mean values are reported as point estimates, instead of the MAP estimates. This is due to the fact that for this example the mean values present the posteriors better than the MAP estimates. One can see that by plotting the corresponding histograms of drawn samples (not shown here).

Table 15: Damage: the identified mean values and the true correlation parameter as well as the identified correlation parameter when the marginal univariate PDFs are the same as the true ones.

μ_E (GPa)	202.2283	μ_{ϵ_f}	0.0013	$\rho_{E\epsilon_f}$	0.7234
s_E^* (GPa)	32.117	$s^*_{\epsilon_f}$	0.0002	$\rho^{\text{true}}_{E\epsilon_f}$	0.7071
$a_1{}_E$ (GPa)	136.0336	$a_{1\epsilon_f}$	0.0008	$\rho^{\text{MAP}}_{E\epsilon_f}$	0.6120
$a_2{}_E$ (GPa)	328.1333	$a_{2\epsilon_f}$	0.0024		

Note that $\rho_{\bullet\bullet}$ denotes the identified correlation coefficient, $\rho^{\text{true}}_{\bullet\bullet}$ the true correlation coefficient and $\rho^{\text{MAP}}_{\bullet\bullet}$ the identified correlation coefficient if the marginal univariate PDFs are the same as the true ones.

Comparing the values in Tables 15 and 16 we see that the identified correlation coefficients are similar. Clearly, the correlation parameter does not depend much on the chosen marginal univariate distributions.

Now, we propagate the PDFs in the type A network models with $h = 0.1$ mm. The resulting scatter plots for the damageable beams are presented in Fig. 32 and summarised in Table 17. It is difficult to say if the scatter plot using the PDF based on truncated Gaussian distributions is better or worse than the scatter plot in which the PDF based on beta distributions is used. On top of that, whether or not the correlation is incorporated has again no influence.

Table 16: Elastoplasticity: the identified mean values and the true correlation parameter as well as the identified correlation parameter when the marginal univariate PDFs are the same as the true ones.

μ_E (GPa)	174.7576	$\mu_{\sigma_{y0}}$	0.2331	μ_H (GPa)	36.7992
s^*_E (GPa)	30.7755	$s^*_{\sigma_{y0}}$	0.0602	s^*_H (GPa)	7.3579
a_{1E} (GPa)	166.3937	$a_{1\sigma_{y0}}$	0.1406	a_{1H} (GPa)	31.9466
a_{2E} (GPa)	305.9041	$a_{2\sigma_{y0}}$	0.3893	a_{2H} (GPa)	84.2107
$\rho_{E\sigma_{y0}}$	0.6665	ρ_{EH}	0.6104	$\rho_{\sigma_{y0}H}$	0.094
$\rho^{\text{true}}_{E\sigma_{y0}}$	0.7071	ρ^{true}_{EH}	0.5	$\rho^{\text{true}}_{\sigma_{y0}H}$	0
$\rho^{\text{MAP}}_{E\sigma_{y0}}$	0.6151	ρ^{MAP}_{EH}	0.6063	$\rho^{\text{MAP}}_{\sigma_{y0}H}$	0.0893

Note that $\rho_{\bullet\bullet}$ denotes the identified correlation coefficient, $\rho^{\text{true}}_{\bullet\bullet}$ the true correlation coefficient and $\rho^{\text{MAP}}_{\bullet\bullet}$ the identified correlation coefficient if the marginal univariate PDFs are the same as the true ones.

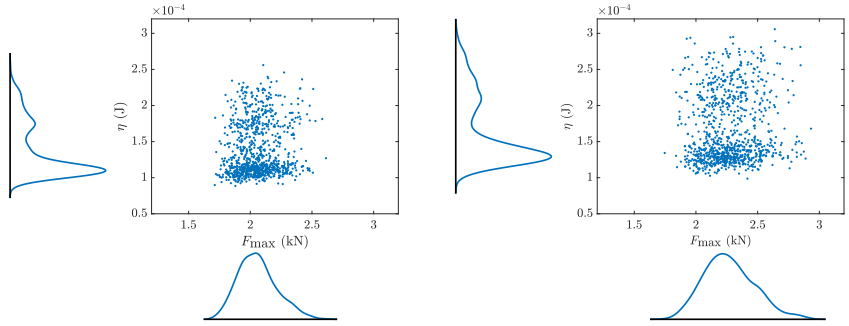

(a) True joint PDF

(b) Beta distribution

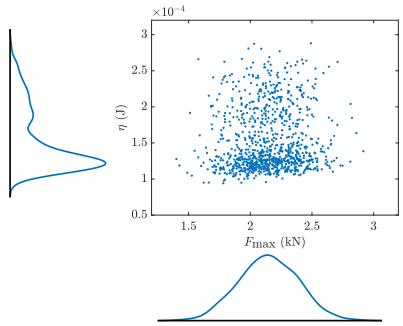

(c) Truncated Gaussian distribution

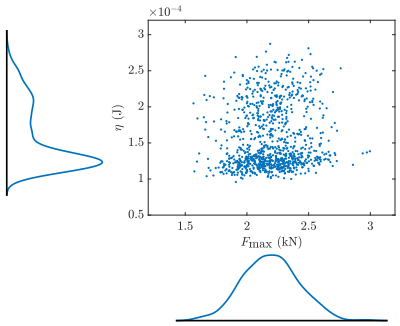

(d) Truncated Gaussian distribution without correlation

Figure 32: Damage: the scatter plots of the maximum force ($F_{\max}$) and dissipated energy (η) for the type A networks with $h = 0.1$ mm. One can see that if the marginal univariate PDFs are not modelled exactly the same as true ones the marcoscale behaviour of the system does not change significantly. Furthermore, we can see that the effect of correlation is not significant too.

Table 17: Damage: the mean values and Pearson correlation coefficient for the type A networks with $h = 0.1$ mm.

$F_{\max}^{\text{mean}}$ (kN)	η^{mean} (J)	$\rho_{F_{\max}\eta}$
True joint PDF		
2.0584	1.3703×10^{-4}	0.1067
Beta distribution		
2.2701	1.647×10^{-4}	0.0734
Truncated Gaussian distribution		
2.1482	1.5264×10^{-4}	0.0626
Truncated Gaussian distribution without correlation		
2.194	1.5688×10^{-4}	0.0876

The results for elastoplasticity are presented in Fig. 33 and Table 18. They show that for elastoplasticity, the influence of selecting the correct marginal univariate PDF is more important, since the results for the truncated Gaussian distribution are less accurate. We also see that the correlation is more important to incorporate (which is clearly in agreement with the results of the previous subsections).

Table 18: Elastoplasticity: the mean values and Pearson correlation coefficients for the type A networks with $h = 0.1$ mm.

k_E^{mean} $(\frac{\text{kN}}{\text{mm}})$	F_{y0}^{mean} (kN)	k_P^{mean} $(\frac{\text{kN}}{\text{mm}})$	$\rho_{k_E F_{y0}}$	$\rho_{k_E k_P}$	$\rho_{F_{y0} k_P}$
True joint PDF					
991.1905	7.2735	205.7121	0.6790	0.4605	-0.0257
Beta distribution					
997.0578	7.2563	206.3549	0.5805	0.5535	0.0605
Truncated Gaussian distribution					
1005.8818	7.8353	210.9785	0.5621	0.3934	0.0130
Truncated Gaussian distribution without correlation					
998.2208	7.3268	205.0491	0.0553	-0.0275	0.0471

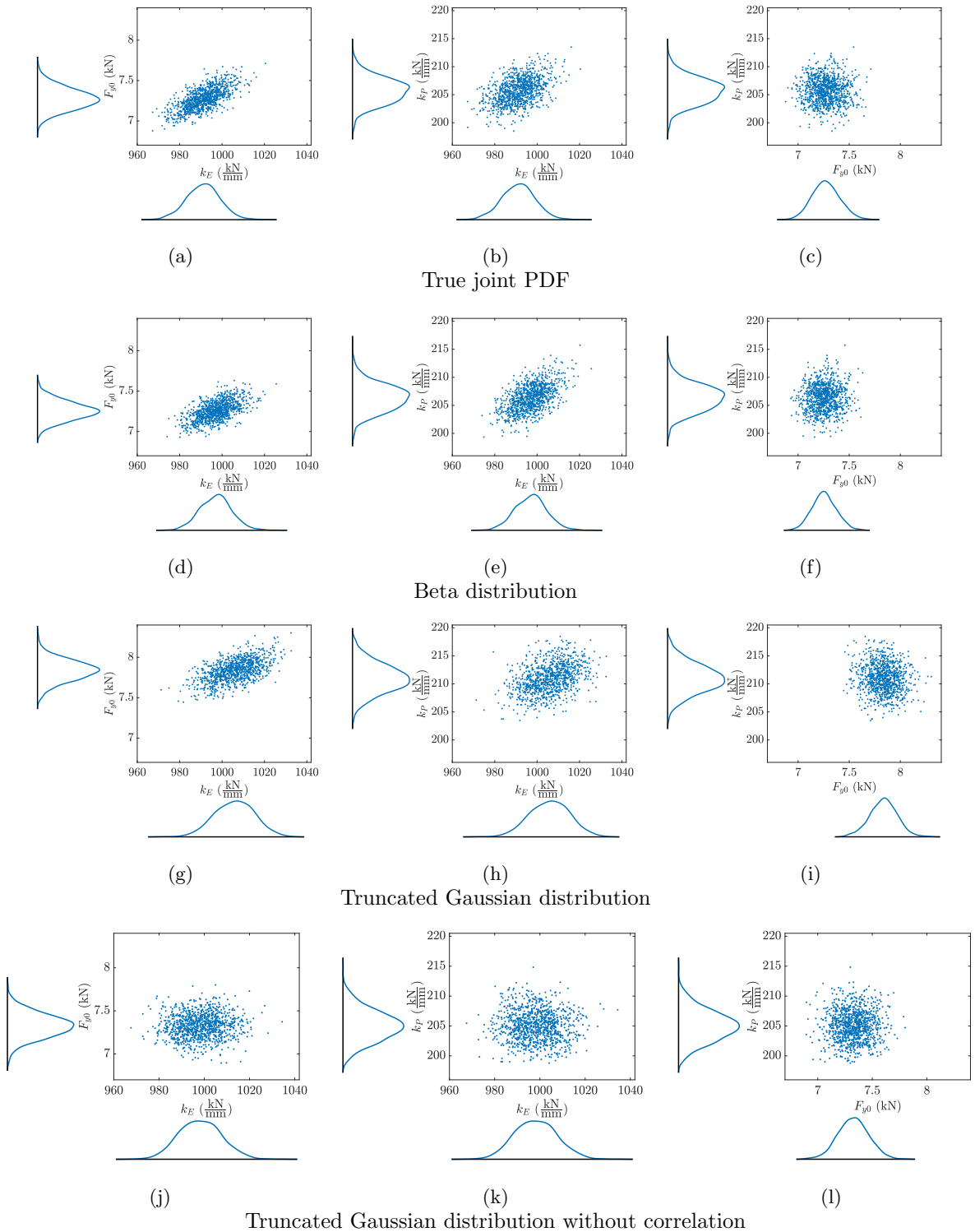

Figure 33: Elastoplasticity: the scatter plots of the systems' equivalent elastic stiffness (k_E), initial yield force (F_{y0}) and plastic stiffness (k_P) for the type A networks with $h = 0.1$ mm. One can see that in this case the effects of marginal univariate PDFs and the correlation are considerable.

5.4. Discussion on the geometrical randomness and systems' parameters correlations

The presented results indicate that an increase of the geometrical randomness results in more pronounced correlations between the system's parameters for elastoplastic constituents, but not for damageable constituents. Consequently, whether or not the material parameters' correlations for elastoplastic constituents are incorporated is less important for an increase of the geometrical randomness. In this subsection, we postulate a reasoning for why an increase of the geometrical randomness results in more pronounced system parameter correlations for the elastoplastic case, but not for the damageable case.

For damageable constituents, we see no correlation between the maximum force and the dissipated energy during the virtual tensile experiments. We believe that the reason for this is as follows. In Fig. 34, we see two schematic illustrations of localisation zones in which the constituents fail. In the left image, we see four short constituents and in the right two long ones. The first failure of a constituent marks the maximum force and is governed by the local strain in a constituent. At the moment at which the first constituent fails, the maximum force for the left image will be roughly twice as large as for the right image, because twice as many constituents are present in the left image.

The dissipated energy on the other hand is the sum of the energies stored in all constituents at the moment at which they fail. In the left image, four constituents will eventually fail, whereas in the right image only two will fail. As the four constituents in the right image are short compared to the two in the right image however, more energy is stored in the constituents on the right and hence, the dissipated energy in the right image will be larger than for the left. In other words, no physical reason is present why the maximum force and dissipated energy are correlated.

For elastoplastic constituents however, we do observe a correlation between the elastic stiffness, yield force and plastic stiffness in the virtual experiments. We again explain this based on the schematic illustrations in Fig. 34. Now however, we consider the localisation zones to consist of the constituents that behave plastically. As four constituents are present in the left image and two in the right image, the elastic stiffness is larger for the left image. At some point, the stress in the constituents will reach their initial yield stress, which is roughly the point that marks the yield force in the virtual experiments. As four constituents are present in the left image and only two in the right, the yield force for the structure in the left image will roughly be twice as large as for the right image. When all constituents have reached their yield stress, the mechanical response of the structure is governed by the plastic stiffness of the constituents. The same reasoning as used for the elastic stiffness can then be used to explain why the plastic stiffness in the left image is roughly twice as large as for the right image.

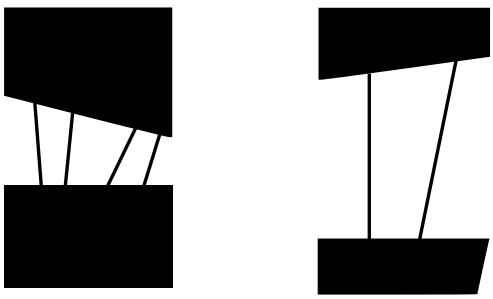

Figure 34: Schematic of two localisation zones in which the constituents break (for damageable constituents) or the constituents behave plastically (for elastoplastic constituents) during the virtual experiments. Left: four short constituents are present in the localisation zone, right: two long constituents are present in the localisation zone.

6. Conclusion

This contribution deals with the issue that different fibres, struts or yarns in fibrous and other discrete materials often have different material properties. We assume that the material properties of each fibre,

strut or yarn are a realisation from some PDF. The question we try to answer is how the parameters of this PDF can be identified with limited experimental means; by testing only 20 constituents instead of hundreds.

We have proposed a four step identification scheme to determine the PDF's parameters. Bayesian inference plays an important role in the identification scheme as it regularises the individual identification problems. When the material parameters of each of the 20 constituents are identified, we first select a univariate PDF for each type of material parameter and identify the parameters of each univariate PDF using the regularisation offered by Bayesian inference. When the parameters of the univariate PDFs are identified, we join them in a single, joint PDF by the use of a copula function. The parameters of the copula need to be identified in turn, for which we again use Bayesian inference.

The presented identification results show that the identified PDFs are accurate representations of the true PDFs. The results also show that incorporating the correlation between the different types of material parameters (via copulas) improves the quality of the identified PDF.

Not only the material randomness is of influence on the macroscale responses of fibrous and other discrete materials however, but also the geometrical randomness. We have therefore also conducted a forward study using random network models in which the different PDFs are used to sample the material parameters of the constituents. These results have indicated that if a perfectly brittle damage model is used, the incorporation of the correlation between the Young's modulus and the failure strain has practically no influence on the accuracy of the predicted PDFs. We have also shown that the amount of geometrical randomness is of no influence. This story changes for elastoplasticity however. The correlation between the material parameters is important to incorporate and becomes more important if the fibre density increases or if the fibre length increases. We have also shown, and explained, that the correlation's influence reduces for an increase of the geometrical randomness.

Acknowledgements

The authors would like to acknowledge the financial support from the University of Luxembourg. The authors are also grateful for the support of the Fonds National de la Recherche Luxembourg DFG-FNR grant INTER/DFG/16/1150192. The numerical results presented in this paper were carried out using the HPC facilities of the University of Luxembourg [59] – see `https://hpc.uni.lu`.

References

[1] P.J. Arnoux, J. Bonnoit, P. Chabrand, M. Jean, M. Pithioux, Numerical damage models using a structural approach: Application in bones and ligaments, The European Physical Journal-Applied Physics 17 (1) (2002) 65–73.

[2] A. Ridruejo, C. González, J. LLorca, Damage micromechanisms and notch sensitivity of glass-fiber non-woven felts: An experimental and numerical study, Journal of the Mechanics and Physics of Solids 58 (10) (2010) 1628–1645.

[3] A. Kulachenko, T. Uesaka, Direct simulations of fiber network deformation and failure, Mechanics of Materials 51 (2012) 1–14.

[4] J. Persson, P. Isaksson, A particlebased method for mechanical analyses of planar fiber-based materials, International Journal for Numerical Methods in Engineering 93 (11) (2013) 1216–1234.

[5] D.V. Wilbrink, L.A.A. Beex, R.H.J. Peerlings, A discrete network model for bond failure and frictional sliding in fibrous materials, International Journal of Solids and Structures 50 (9) (2013) 1354–1363.

[6] L.A.A. Beex, R.H.J. Peerlings, M.G.D. Geers, A multiscale quasicontinuum method for lattice models with bond failure and fiber sliding, Computer Methods in Applied Mechanics and Engineering 269 (2014) 108 –122.

[7] E. Bosco, R.H.J. Peerlings, M.G.D. Geers, Predicting hygro-elastic properties of paper sheets based on an idealized model of the underlying fibrous network, International Journal of Solids and Structures 56-57 (2015) 43–52.

[8] M. Delincé, F. Delannay, Elastic anisotropy of a transversely isotropic random network of interconnected fibres: Non-triangulated network model, Acta Materialia 52 (4) (2004) 1013–1022.

[9] X. Badiche, S. Forest, T. Guibert, Y. Bienvenu, J.D. Bartout, P. Ienny, M. Croset, H. Bernet, Mechanical properties and non-homogeneous deformation of open-cell nickel foams: Application of the mechanics of cellular solids and of porous materials, Materials Science and Engineering: A 289 (1) (2000) 276–288.

[10] A. Jung, L.A.A. Beex, S. Diebels, S.P.A. Bordas, Open-cell aluminium foams with graded coatings as passively controllable energy absorbers, Materials & Design 87 (2015) 36–41.

[11] S. Gao, B. Liang, E. Vidal-Salle, Development of a new 3D beam element with section changes: The first step for large scale textile modelling, Finite Elements in Analysis and Design 104 (2015) 80–88.

[12] B.B. Boubaker, B. Haussy, J.F. Ganghoffer, Discrete woven structure model: Yarn-on-yarn friction, Comptes Rendus Mécanique 335 (3) (2007) 150–158.

[13] L.A.A. Beex, R.H.J. Peerlings, K. van Os, M.G.D. Geers, The mechanical reliability of an electronic textile investigated using the virtual-power-based quasicontinuum method, Mechanics of Materials 80 (2015) 52–66.

[14] G. Argento, M. Simonet, C.W.J. Oomens, F.P.T. Baaijens, Multi-scale mechanical characterization of scaffolds for heart valve tissue engineering, Journal of Biomechanics 45 (16) (2012) 2893–2898.

[15] A.M. Sastry, X. Cheng, C.W. Wang, Mechanics of stochastic fibrous networks, Journal of Thermoplastic Composite Materials 11 (3) (1998) 288–296.

[16] C.W. Wang, L. Berhan, A.M. Sastry, Structure, mechanics and failure of stochastic fibrous networks: Part I-microscale considerations, Journal of Engineering Materials and Technology, 122 (4) (2000) 450–459.

[17] C.A. Bronkhorst, Modelling paper as a two-dimensional elasticplastic stochastic network, International Journal of Solids and Structures 40 (20) (2003) 5441–5454.

[18] H. Hatami-Marbini, R.C. Picu, Scaling of nonaffine deformation in random semiflexible fiber networks, Physical Review E 77 (2008) 062103.

[19] R.C. Picu, Mechanics of random fiber networks-a review, Soft Matter 7 (2011) 6768–6785.

[20] A.S. Shahsavari, R.C. Picu, Size effect on mechanical behavior of random fiber networks, International Journal of Solids and Structures 50 (20) (2013) 3332–3338.

[21] E. Ban, V.H. Barocas, M.S. Shephard, C.R. Picu, Effect of fiber crimp on the elasticity of random fiber networks with and without embedding matrices, Journal of Applied Mechanics 83 (4) (2016) 041008–041008–7.

[22] T.H. Le, P.J.J. Dumont, L. Orgéas, D. Favier, L. Salvo, E. Boller, X-ray phase contrast microtomography for the analysis of the fibrous microstructure of SMC composites, Composites Part A: Applied Science and Manufacturing 39 (1) (2008) 91–103.

[23] P. Latil, L. Orgéas, C. Geindreau, P.J.J. Dumont, S.R. du Roscoat, Towards the 3D in situ characterisation of deformation micro-mechanisms within a compressed bundle of fibres, Composites Science and Technology 71 (4) (2011) 480–488.

[24] R.M. Sencu, Z. Yang, Y.C. Wang, P.J. Withers, C. Rau, A. Parson, C. Soutis, Generation of micro-scale finite element models from synchrotron X-ray CT images for multidirectional carbon fibre reinforced composites, Composites Part A: Applied Science and Manufacturing 91 (2016) 85–95.

[25] R.S. Seth, D.H. Page, The stress-strain curve of paper, in: J. Brander (Ed.), The role of fundamental research in paper making: Transactions of the symposium held at Cambridge, Mechanical Engineering Publications Ltd., London, 1983, pp. 421–452.

[26] A. Jung, S. Diebels, A. Koblischka-Veneva, J. Schmauch, A. Barnoush, M.R. Koblischka, Microstructural analysis of electrochemical coated open-cell metal foams by EBSD and nanoindentation, Advanced Engineering Materials 16 (1) (2013) 15–20.

[27] J. Isenberg, Progressing from least squares to Bayesian estimation, in: Proceedings of the 1979 ASME design engineering technical conference, New York, 1979, pp. 1–11.

[28] K.F. Alvin, Finite element model update via bayesian estimation and minimization of dynamic residuals, AIAA journal 35 (5) (1997) 879–886.

[29] J.L. Beck, L.S. Katafygiotis, Updating models and their uncertainties. I: Bayesian statistical framework, Journal of Engineering Mechanics 124 (4) (1998) 455–461.

[30] T. Marwala, S. Sibusiso, Finite element model updating using Bayesian framework and modal properties, Journal of Aircraft 42 (1) (2005) 275–278.

[31] C. Gogu, R. Haftka, R.L. Riche, J. Molimard, A. Vautrin, Introduction to the Bayesian approach applied to elastic constants identification, AIAA journal 48 (5) (2010) 893–903.

[32] P.S. Koutsourelakis, A novel Bayesian strategy for the identification of spatially varying material properties and model validation: An application to static elastography, International Journal for Numerical Methods in Engineering 91 (3) (2012) 249–268.

[33] T.C. Lai, K.H. Ip, Parameter estimation of orthotropic plates by Bayesian sensitivity analysis, Composite Structures 34 (1) (1996) 29–42.

[34] F. Daghia, S. de Miranda, F. Ubertini, E. Viola, Estimation of elastic constants of thick laminated plates within a Bayesian framework, Composite Structures 80 (3) (2007) 461–473.

[35] J.M. Nichols, W.A. Link, K.D. Murphy, C.C. Olson, A Bayesian approach to identifying structural nonlinearity using free-decay response: Application to damage detection in composites, Journal of Sound and Vibration 329 (15) (2010) 2995–3007.

[36] C. Gogu, W. Yin, R. Haftka, P. Ifju, J. Molimard, R. Le Riche, A. Vautrin, Bayesian identification of elastic constants in multi-directional laminate from moiré interferometry displacement fields, Experimental Mechanics 53 (4) (2013) 635–648.

[37] T. Most, Identification of the parameters of complex constitutive models: Least squares minimization vs. Bayesian updating, in: D. Straub (Ed.), Reliability and optimization of structural systems, CRC press, 2010, pp. 119–130.

[38] H. Rappel, L.A.A. Beex, L. Noels, S.P.A. Bordas, Identifying elastoplastic parameters with Bayes theorem considering output error, input error and model uncertainty, Probabilistic Engineering Mechanics doi:https://doi.org/10.1016/j.probengmech.2018.08.004.

[39] H. Rappel, L.A.A. Beex, J.S. Hale, L. Noels, S.P.A. Bordas, A tutorial on Bayesian inference to identify material parameters in solid mechanics, Archives of Computational Methods in Engineering doi:10.1007/s11831-018-09311-x.

[40] M. Muto, J.L. Beck, Bayesian updating and model class selection for hysteretic structural models using stochastic simulation, Journal of Vibration and Control 14 (1-2) (2008) 7–34.

[41] P. Liu, S. K. Au, Bayesian parameter identification of hysteretic behavior of composite walls, Probabilistic Engineering Mechanics 34 (2013) 101–109.

[42] D.D. Fitzenz, A. Jalobeanu, S.H. Hickman, Integrating laboratory creep compaction data with numerical fault models: A Bayesian framework, Journal of Geophysical Research: Solid Earth 112 (B8), B08410.

[43] W.P. Hernandez, F.C.L. Borges, D.A. Castello, N. Roitman, C. Magluta, Bayesian inference applied on model calibration of fractional derivative viscoelastic model, in: V. Steffen Jr, D.A. Rade, W.M. Bessa (Eds.), DINAME 2015-Proceedings of the XVII International symposium on dynamic problems of mechanics, Natal, 2015.

[44] H. Rappel, L.A.A. Beex, S.P.A. Bordas, Bayesian inference to identify parameters in viscoelasticity, Mechanics of Time-Dependent Materials.
URL `https://doi.org/10.1007/s11043-017-9361-0`

[45] C. Genest, K. Ghoudi, L.P. Rivest, A semiparametric estimation procedure of dependence parameters in multivariate families of distributions, Biometrika 82 (3) (1995) 543–552.

[46] C.M. Bishop, Pattern recognition and machine learning, Information Science and Statistics, Springer, New York, 2006.

[47] W. Hürlimann, Fitting bivariate cumulative returns with copulas, Computational Statistics & Data Analysis 45 (2) (2004) 355–372.

[48] O. Roch, A. Alegre, Testing the bivariate distribution of daily equity returns using copulas. An application to the Spanish stock market, Computational Statistics & Data Analysis 51 (2) (2006) 1312–1329.

[49] R.d.S. Silva, H.F. Lopes, Copula, marginal distributions and model selection: A Bayesian note, Statistics and Computing 18 (3) (2008) 313–320.

[50] J.C. Simo, T.J.R. Hughes, Computational inelasticity, Springer Science & Business Media, New York, 2000.

[51] J. Kaipio, E. Somersalo, Statistical and computational inverse problems, Vol. 160, Springer, New York, 2006.

[52] S. Brooks, A. Gelman, G. Jones, X.L. Meng, Handbook of Markov chain Monte Carlo, CRC press, 2011.

[53] J.L. Beck, Bayesian system identification based on probability logic, Structural Control and Health Monitoring 17 (7) (2010) 825–847.

[54] R.B. Nelsen, An introduction to copulas, Springer Science & Business Media, 2007.

[55] M. Sklar, Fonctions de répartition à n dimensions et leurs marges, Université Paris 8, 1959.

[56] Y. Noh, K.K. Choi, I. Lee, Identification of marginal and joint CDFs using Bayesian method for RBDO, Structural and Multidisciplinary Optimization 40 (1) (2009) 35.

[57] P. X. Song, Multivariate dispersion models generated from Gaussian copula, Scandinavian Journal of Statistics 27 (2) (2000) 305–320.

[58] H. Haario, E. Saksman, J. Tamminen, Adaptive proposal distribution for random walk Metropolis algorithm, Computational Statistics 14 (3) (1999) 375–396.

[59] S. Varrette, P. Bouvry, H. Cartiaux, F. Georgatos, Management of an academic HPC cluster: The UL experience, in: Proc. of the 2014 Intl. Conf. on High Performance Computing & Simulation (HPCS 2014), IEEE, Bologna, Italy, 2014, pp. 959–967.